Low-order Prandtl-Glauert-Lorentz based Absorbing Boundary Conditions for solving the convected Helmholtz equation with Discontinuous Galerkin methods

Hélène Barucq, Nathan Rouxelin, Sébastien Tordeux

Low-order Prandtl-Glauert-Lorentz based Absorbing Boundary Conditions for solving the convected Helmholtz equation with Discontinuous Galerkin methods

Hélène Barucq[a], Nathan Rouxelin[a,b,*], Sébastien Tordeux[a]

[a] *MAKUTU, Inria, TotalEnergies, Université de Pau et des Pays de l'Adour, CNRS, France*
[b] *Laboratoire de Mathématiques de l'INSA, INSA Rouen–Normandie, Normandie-Université, France*

Abstract

We construct Absorbing Boundary Conditions (ABCs) for the convected Helmholtz equation that are easy to implement in a Hybridizable Discontinuous Galerkin (HDG) formulation. The construction is based upon the Prandtl-Glauert-Lorentz map which transforms the convected Helmholtz equation into the regular Helmholtz equation. The new ABCs are thus issued from classical Bayliss-Gunztburger-Turkel ABCs and are valid for carrier flows that vary inside the computational domain but become uniform far away from the source. They lead to accurate numerical results for low and intermediate Mach numbers using a HDG formulation with the acoustic potential and the total flux as unknowns.

Keywords: convected Helmholtz equation, Absorbing Boundary Conditions, ABC, Prandtl Glauert Lorentz transformation

Introduction

The study of acoustic waves in the presence of a flow is involved in many applications. The work presented here is motivated by the objective to develop an advanced computational framework to simulate acoustic waves propagating at shallow depths in the sun and in its atmosphere. In [Rou21], the time harmonic Galbrun equations have been studied first and numerical experiments illustrate that in the presence of a flow, the simulations can be unstable if continuous finite elements are used. From this came the idea to develop a computational library based on less regular approximation spaces in order to better respect the regularity properties of the solution of the Galbrun equations. Our choice was to implement a Discontinuous Galerkin (DG) method and we opted for the development of Hybridizable DG (HDG) formulations in order to work with discrete systems of reasonable size. A direct DG approximation leads indeed to systems whose size is largely superior to the one obtained

*Corresponding author
Email addresses: helene.barucq@inria.fr (Hélène Barucq), nathan.rouxelin@inria.fr (Nathan Rouxelin), sebastien.tordeux@inria.fr (Sébastien Tordeux)

with a continuous finite element approximation, even more so if we use high orders of approximation. The advantage of HDG formulations is that they are constructed as mixed DG methods to which static condensation can be applied. The global system is thus defined to compute an auxiliary unknown defined only on the skeleton of the mesh and the global solution is reconstructed at low cost by solving in parallel local problems of very small size. For a nice introduction to HDG methods, we refer to [KSC12].
As a first step, we consider here the convected Helmholtz equation and as in helioseismology the waves propagate in an infinite medium, we address the question of limiting externally the computational domain in the purpose of using finite element methods. Domain truncation is important for computational wave dynamics, and the two most popular truncation techniques are:

- Perfectly Matched Layers (PMLs), introduced in [Ber94]; they surround the domain of interest and involve a damping parameter introduced in the equations in such a way that (i) waves are perfectly transmitted across the interface between the real medium and the artificial layer and (ii) the waves are sufficiently absorbed in the layer to avoid the possible back propagation of waves from the layer;

- *Absorbing Boundary Conditions (ABCs)*, introduced in [EM77]; they select waves outgoing to the computational domain limited externally with a boundary meant to be transparent in an ideal world. Exact ABCs are often expressed in terms of non-local operators and finding local approximation of those operators is a problem that remains difficult and yet crucial to perform large-scale simulations with reasonable computational costs.

Regarding PMLs, it has been shown that standard PMLs might be unstable because of the possible existence of back-propagating modes. In [BDL04], stabilized PMLs have been derived for the time-harmonic convected Helmholtz equation in a duct with a uniform flow, adapting ideas formerly developed in [HN02] and [Hu01] for time-dependent problems. In a very recent work [MBAG21], Marchner et al. have proposed a stabilized PML for the convected Helmholtz equation following the approach in [DDMT11] of applying the *Prandtl-Glauert-Lorentz transformation* (PGL) to remove the external flow to end up with the standard Helmholtz equation for which stable PMLs exist. It is worth noting that in [DDMT11], the PML is constructed for the advective acoustic equation when the velocity of the fluid is parallel to a particular direction while [MBAG21] only assumes the flow is uniform and subsonic.
In this paper, we focus on the construction of ABCs for the convected Helmholtz equation which can be implemented easily in the different HDG formulations that we have introduced in a previous work [BRT21]. To the best of our knowledge, this has not yet been done. Actually, high-order ABCs for the convected Helmholtz equation have been constructed and implemented in finite difference schemes and continuous finite element formulation [HHT03, BGH10]. In [HHT03], the construction is based upon a multipole expansion of outgoing solutions and high-order conditions are obtained from the combination of low-order derivatives thanks to auxiliary unknowns. The resulting conditions are implemented

in a finite difference scheme, assuming the flow is uniform outside a bounded region and aligns with a coordinate axis. In [BGH10], the construction is extended to anisotropic and subsonically convective media in the case of rectangular artificial boundary, numerical experiments with finite elements being reserved to the anisotropic case. Following the original idea of [HHT03], complete absorbing (or radiation) boundary conditions have been proposed in [Kim14] for the case of the convected Helmholtz equation with a uniform flow in a waveguide. Very recently, radiation boundary conditions have been constructed by applying a micro-local factorization of the convected Helmholtz operator when the flow is aligned with a coordinate axis [MAGB21]. The construction of an exact ABC is also feasible from a theoretical point of view but it involves a non-local operator whose discretization induces an additional computational load. Some attempts have been carried out, for instance in [CES14, BCD+14] where the non-local operator is approximated with an integral equation coupled with a volume finite element solution. Another approach consists in using infinite elements (or wave-envelope elements) as it is proposed in [AH01] for the convected Helmholtz equation. To deal with the unbounded nature of the domain, the solution is computed as a truncated multipole expansion outside a convex bounded domain which contains the sources. Then the solution is computed in conjunction with finite elements inside the bounded domain. It turns out that the coupling with DG approximations inside the bounded region containing the sources is still a challenging problem that deserves a work in itself.

Herein, we construct a family of local ABCs based on the *Prandtl-Glauert-Lorentz transformation* for the convected Helmholtz equation. These conditions are meant to be integrated in HDG discretizations. Hence they are constructed for the first-order formulation of the convected Helmholtz equation. They are constructed from the ABCs formerly derived for the standard Helmholtz equation in [BGT82] using the *Prandtl-Glauert-Lorentz transformation*. Without saying so, it is worth mentioning that this idea has already been exploited in [BT82] for a convective wave equation with a constant free stream flow. That the flow is constant probably explains that the authors did not introduce the *Prandtl-Glauert-Lorentz transformation* as the change of variables to go from the convective wave equation to the acoustic wave equation was quite natural. Finally, it is important to note that the *Prandtl-Glauert-Lorentz transformation* is only used to compute the coefficients on the artificial boundary. Hence the new ABCs are valid for a flow that varies inside the domain but becomes uniform at infinity. Numerical experiments based upon the solution of a HDG formulation (see [BRT21]) illustrate the efficiency of the new ABCs for low and intermediate Mach numbers.

This paper is organized as follows:

- In Section 1, we recall some results about the convected Helmholtz equation and precisely state the assumptions under which the new ABCs are derived.
- In Section 2, we use the *Prandtl-Glauert-Lorentz transformation* to construct the new ABCs.
- In Section 3, we present numerical results to illustrate the performance of the new

ABCs. Only low-order conditions are investigated as the integration of high-order conditions in HDG formulations is still challenging.

1. Model problem and geometric settings

In this section, we introduce the *convected Helmholtz equation* and recall some of its properties. We also precisely state the assumptions under which the new Absorbing Boundary Condition are constructed.

1.1. Equation and carrier flow

We consider the following *convected Helmholtz equation*

$$\rho_0 \left(-\omega^2 p - 2i\omega \boldsymbol{v_0} \cdot \nabla p + \boldsymbol{v_0} \cdot \nabla[\boldsymbol{v_0} \cdot \nabla p]\right) - \operatorname{div}\left(\rho_0 c_0^2 \nabla p\right) = s, \tag{1}$$

where p is the acoustic potential, $\boldsymbol{v_0}$ is the velocity of the carrier flow, c_0 is the adiabatic sound speed, ρ_0 is the density of the flow and s is the acoustic source.

In this paper, we use the following convention for time-harmonic solutions

$$\mathsf{p}(\boldsymbol{x}, t) = p(\boldsymbol{x}, \omega) e^{-i\omega t}.$$

To make the notations lighter, the $e^{-i\omega t}$ factor is omitted, and, in this paper vectors are assumed to be column vectors.

The physical perturbations of pressure p' and of velocity $\boldsymbol{v}'$ can be recovered from the potential using the following relations

$$p' = -\rho_0 c_0 (-i\omega + \boldsymbol{v_0} \cdot \nabla) p, \quad \text{and} \quad \boldsymbol{v}' = -c_0 \nabla p.$$

As usual in acoustics, this model is obtained thanks to a linearization process and is therefore only valid for small perturbations.

As there are several ways to write the convected Helmholtz equation, see [Pie90], we have chosen the simple form (1) as a model problem for this paper. The construction of the ABCs presented here can then be adapted to the other forms of the equation without major difficulties. In particular, the results for the *velocity potential formulation*

$$(-i\omega + \boldsymbol{v_0} \cdot \nabla) \frac{1}{c_0^2} (-i\omega + \boldsymbol{v_0} \cdot \nabla) \varphi - \frac{1}{\rho_0} \operatorname{div}(\rho_0 \nabla \varphi) = s, \tag{2}$$

will also be stated.

In this paper we will make the following usual assumptions on the carrier flow:

Assumption 1 (Incompressible flow). The density of the flow ρ_0 is uniform. Upon non-dimensionalization we can always choose $\rho_0 \equiv 1$. The velocity $\boldsymbol{v_0}$ satisfies the following incompressibility equation

$$\operatorname{div}(\boldsymbol{v_0}) = 0.$$

Remark 1.1. Taking other values of ρ_0 into account only amounts to small changes in the construction of the ABCs. Notice that if ρ_0 is allowed to vary inside the computational domain but becomes equal to one close to the boundary, then ASSUMPTION 1 should be replaced with the usual *mass conservation equation*

$$\operatorname{div}(\rho_0 \boldsymbol{v_0}) = 0.$$

Assumption 2 (Subsonic flow). The carrier flow is subsonic, *ie.*

$$\inf\left(c_0^2 - |\boldsymbol{v_0}|^2\right) > 0.$$

We introduce the matrix

$$\boldsymbol{K_0} := c_0^2 \mathbf{Id} - \boldsymbol{v_0}\boldsymbol{v_0}^T, \tag{3}$$

where $\mathbf{Id}$ denotes the identity matrix. Then, using ASSUMPTION 1, (1) can be rewritten as

$$-\omega^2 p - \operatorname{div}(\boldsymbol{K_0}\nabla p + 2i\omega p \boldsymbol{v_0}) = s. \tag{4}$$

The quantity

$$\boldsymbol{\sigma} := -\boldsymbol{K_0}\nabla p - 2i\omega p \boldsymbol{v_0} \tag{5}$$

is called the *total flux* and allows to rewrite the convected Helmholtz equation as a first-order system conducive to get a mixed DG formulation. Actually, it is showed in [BRT21] that the HDG method for solving the following first-order system

$$\begin{aligned} \boldsymbol{\sigma} + \boldsymbol{K_0}\nabla p + 2i\omega p \boldsymbol{v_0} &= 0, \\ -\omega^2 p + \operatorname{div}(\boldsymbol{\sigma}) &= s, \end{aligned}$$

has some attractive properties when compared to other HDG methods for the convected Helmholtz equation. In particular it provides an optimal order of convergence and does not depend on the choice of a penalization parameter, as an optimal penalization parameter can be computed a priori. The aim of this paper is therefore to construct ABCs that takes both effects of wave propagation and convection into account and that are easy to implement in a HDG solver.

1.2. Geometric assumptions for the background flow

As the Absorbing Boundary Conditions will be constructed using the *Prandtl-Glauert-Lorentz transformation*, the background flow must be locally uniform around the artificial boundary. We therefore make the following assumption.

Assumption 3 (Uniform flow outside a compact). There exists a compact K such that $\boldsymbol{v_0}$ and c_0 are constant outside K.

ASSUMPTION 3 is a reasonable assumption: in practice we can always assume that the background flow becomes uniform if the artificial boundary is located far away from the acoustic source. It is also worth noticing that a similar assumption is usually used to derive ABCs for the standard Helmholtz equation. A sketch of this configuration is given in FIGURE 1.

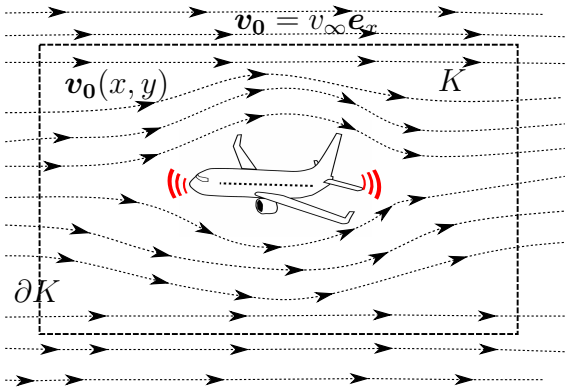

Figure 1: Flow around an aircraft, the flow is uniform outside K

2. Prandtl-Glauert-Lorentz transformation and approximate ABCs

In this section we introduce the *Prandtl-Glauert-Lorentz transformation* on which the construction of the new ABCs is based. We recall that the *Prandtl-Glauert-Lorentz transformation* maps the convected Helmholtz equation into the standard one. We then show how the boundary conditions are transformed under this change of coordinates. Finally we construct new ABCs for the convected Helmholtz equation in 2D.

2.1. Prandtl-Glauert-Lorentz transformation

We define the *Lorentz factor*

$$\alpha := \sqrt{1 - M^2},$$

where M is the Mach-number defined as

$$\boldsymbol{M_0} := \frac{1}{c_0}\boldsymbol{v_0}, \quad \text{and} \quad M^2 := \boldsymbol{M_0}^T \boldsymbol{M_0}.$$

Following [HPN19, MBAG21, Cha00], we use the following frequency-domain transformation

$$\widetilde{\omega} = \frac{\omega}{\alpha} \quad ; \quad \widetilde{\boldsymbol{x}} = \boldsymbol{A}\boldsymbol{x} := \left(\mathbf{Id} + \frac{1}{\alpha(1+\alpha)}\boldsymbol{M_0}\boldsymbol{M_0}^T\right)\boldsymbol{x}. \tag{6}$$

Depending on the sources, it can be called *Lorentz transformation*, *Prandtl-Glauert transformation* or sometimes *Prandtl-Glauert-Lorentz transformation*. The term *Lorentz transformation* is used as this transformation is close to the Lorentz transformation arising in special relativity.

Using the *Sherman-Morrisson formula* [SM50], it is easy to show that

$$\boldsymbol{A}^{-1} = \mathbf{Id} - \frac{1}{1+\alpha}\boldsymbol{M_0}\boldsymbol{M_0}^T.$$

We can therefore write the inverse *Prandtl-Glauert-Lorentz transformation*

$$\omega = \alpha\widetilde{\omega} \quad ; \quad \boldsymbol{x} = \boldsymbol{A}^{-1}\widetilde{\boldsymbol{x}} := \left(\mathbf{Id} - \frac{1}{1+\alpha}\boldsymbol{M_0}\boldsymbol{M_0}^T\right)\widetilde{\boldsymbol{x}}.$$

A direct computation, see [Rou21, Lemma 4.2.2], allows to prove the

Lemma 1. *Let p be a solution of (1). If c_0 and $\boldsymbol{v_0}$ are constant, then $\widetilde{p}$ defined by*

$$\widetilde{p}(\widetilde{\boldsymbol{x}}, \widetilde{\omega}) = \alpha \exp\left[i \frac{\omega}{\alpha^2 c_0} \boldsymbol{M_0} \cdot \boldsymbol{x}\right] p(\boldsymbol{x}, \omega) \tag{7}$$

satisfies the standard Helmholtz equation

$$-\widetilde{\omega}^2 \widetilde{p} - c_0^2 \widetilde{\Delta} \widetilde{p} = \widetilde{s},$$

where $\widetilde{\Delta}$ is the Laplace operator in Prandtl-Glauert-Lorentz coordinates and

$$\widetilde{s}(\widetilde{\boldsymbol{x}}, \widetilde{\omega}) = \alpha \exp\left[i\omega \frac{\boldsymbol{M_0} \cdot \boldsymbol{x}}{\alpha^2 c_0}\right] s(\boldsymbol{x}, \omega).$$

The *Prandtl-Glauert-Lorentz transformation* will be used to construct ABCs for the convected Helmholtz equation. The validity of this approach is ensured by the following lemma whose proof is postponed to Appendix A.

Lemma 2. *The* Prandtl-Glauert-Lorentz transformation *maps outgoing solutions of the convected Helmholtz equation to outgoing solutions of the Helmholtz equation.*

2.2. Transformation of the boundary condition

We now introduce a boundary Σ, the so-called artificial boundary, which limits a region including the support of the acoustic source and thus defines a bounded computational domain $\mathcal{O}$. The ABC is then set on the artificial boundary Σ. We also denote $\widetilde{\Sigma}$ the artificial boundary in Lorentz coordinates. For simplicity, we will choose a circle centered on the origin for $\widetilde{\Sigma}$, Σ will therefore be an ellipse. An example is depicted on Figure 2. More precisely, the following lemma holds.

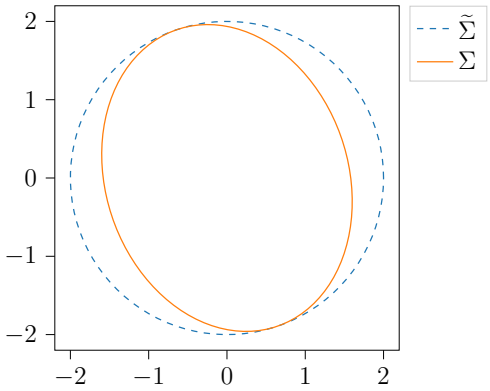

Figure 2: Σ and $\widetilde{\Sigma}$ for $\boldsymbol{M_0} = [0.6\ 0.2]^T$ and $R = 2$

Lemma 3. *Let $R > 0$. If the artificial boundary in Lorentz coordinates satisfies*

$$\widetilde{\Sigma} = \left\{\widetilde{\boldsymbol{x}} \;\middle|\; |\widetilde{\boldsymbol{x}}|^2 = R^2\right\} = \left\{\widetilde{\boldsymbol{x}} = R\left(\cos(t)\boldsymbol{e}_x + \sin(t)\boldsymbol{e}_y\right) \;\middle|\; t \in [0, 2\pi)\right\},$$

then the artificial boundary in physical coordinates satisfies

$$\Sigma = \left\{\boldsymbol{x} \;\middle|\; |\boldsymbol{A}\boldsymbol{x}| = R^2\right\} = \left\{\boldsymbol{x} = R\left(\cos(t)\boldsymbol{A}_1 + \sin(t)\boldsymbol{A}_2\right) \;\middle|\; t \in [0, 2\pi)\right\},$$

where $\boldsymbol{A}_1$ and $\boldsymbol{A}_2$ are the first and second columns of $\boldsymbol{A}^{-1}$.

Remark 2.1. At first glance, the other choice (taking a circle in physical coordinates and an ellipse in Lorentz coordinates) may seem more natural. However ABCs for the Helmholtz equation on an ellipsoidal boundary are more complicated to implement. If they are derived using an analytical point of view, those ABCs are expressed using special functions whose numerical evaluation may be unstable, see [BST12, Sai08]. On the other hand, if a geometric point of view is used, the resulting ABCs involve curvature operators that are difficult to approximate, see [BGT82, ABB99].

We will now state and prove the main result of this paper.

Theorem 4. *Let p be the solution of*

$$-\omega^2 p - \operatorname{div}\left(\boldsymbol{K_0}\nabla p + 2i\omega p \boldsymbol{v_0}\right) = s, \qquad \text{in } \mathcal{O}, \tag{8a}$$

$$\boldsymbol{\sigma}\cdot\boldsymbol{n} + \mathcal{Z}p = 0, \qquad \text{on } \Sigma, \tag{8b}$$

where $\boldsymbol{K_0}$ is defined by (3) and scales like c_0^2, and $\boldsymbol{\sigma}$ is the total flux defined by (5). Then if $\boldsymbol{v_0}$ and c_0 are constant, and if $\widetilde{p}$ is defined by (7), then $\widetilde{p}$ is a solution to

$$-\widetilde{\omega}^2\widetilde{p} - c_0^2\widetilde{\Delta}\widetilde{p} = \widetilde{s}, \qquad \text{in } \widetilde{\mathcal{O}}, \tag{9a}$$

$$\partial_{\widetilde{\boldsymbol{n}}}\widetilde{p} + \widetilde{\mathcal{Z}}\widetilde{p} = 0, \qquad \text{on } \widetilde{\Sigma}, \tag{9b}$$

if the boundary operators satisfy

$$\mathcal{Z}(\boldsymbol{x},\omega) = -c_0^2|\boldsymbol{A}^{-T}\boldsymbol{n}|\widetilde{\mathcal{Z}}(\widetilde{\boldsymbol{x}},\widetilde{\omega}) + i\omega\boldsymbol{v_0}\cdot\boldsymbol{n}. \tag{10}$$

Furthermore the problems (8a)–(8b) and (9a)–(9b) are both well-posed.

Remark 2.2. We can notice that $\mathcal{Z}$ and $\widetilde{\mathcal{Z}}$ do not have the same physical dimension. This is not a consequence of the *Prandtl-Glauert-Lorentz transformation*, but it comes from the choice of unknown for the convected Helmholtz equation. Indeed, ABCs based on $\boldsymbol{\sigma}\cdot\boldsymbol{n}+\mathcal{Z}p$ for the convected Helmholtz equation should be interpreted as $-c_0^2\partial_{\boldsymbol{n}}p + \mathcal{Z}p$, whereas most ABCs for the standard Helmholtz equation are written as $\partial_{\boldsymbol{n}}p + \mathcal{Z}p$. This explains both the minus sign and the difference in dimensions between the coefficient. We recall that we have chosen to use $\boldsymbol{\sigma}$ because it is convenient for constructing mixed finite element methods, see [BRT21].

Remark 2.3. Notice that even if Theorem 4 is stated for a uniform flow, the new Absorbing Boundary Conditions can be used in the more general case described by Assumption 3. Indeed as the *Prandtl-Glauert-Lorentz transformation* will only be used to construct the boundary operator, the carrier flow only needs to be locally uniform close to the artificial boundary.

Remark 2.4. ABCs for the standard Helmholtz equation satisfy $\mathfrak{Im}\widetilde{\mathcal{Z}} < 0$, using (10) we can see that ABCs for the convected Helmholtz equation satisfy $\mathfrak{Im}\mathcal{Z} - \omega\boldsymbol{v_0}\cdot\boldsymbol{n} > 0$. This can be understood as $\boldsymbol{\sigma}\cdot\boldsymbol{n}$ should be interpreted as $-\partial_{\boldsymbol{n}}p$. If the signs are reversed, then the boundary conditions select incoming waves instead of outgoing ones.

Remark 2.5. Equation (10) can also be written as

$$\mathcal{Z}(\boldsymbol{x},\omega) = -c_0^2\left(|\boldsymbol{A}^{-T}\boldsymbol{n}|\widetilde{\mathcal{Z}}(\widetilde{\boldsymbol{x}},\widetilde{\omega}) - i\frac{\omega}{c_0}\boldsymbol{M_0}\cdot\boldsymbol{n}\right),$$

however we have chosen to use the formulation (10) as it is closer the implementation choices that were performed in [BRT21].

Proof (of Theorem 4). Let us now focus on the boundary conditions (8b) and (9b). This is adapted from [HPN19, Sec. 3].

We assume that Σ and $\widetilde{\Sigma}$ have the following cartesian equations

$$\Sigma : \{\Phi(\boldsymbol{x}) = 0\} \quad \text{and} \quad \widetilde{\Sigma} : \left\{\widetilde{\Phi}(\widetilde{\boldsymbol{x}}) = 0\right\}.$$

Step 1:

Because of the chain rule, we have the following relationship between their normal directions

$$\nabla\Phi = \frac{\partial\Phi}{\partial\boldsymbol{x}} = \frac{\partial\widetilde{\boldsymbol{x}}}{\partial\boldsymbol{x}}\frac{\partial\widetilde{\Phi}}{\partial\widetilde{\boldsymbol{x}}} = \boldsymbol{A}^T\widetilde{\nabla}\widetilde{\Phi}$$

Let $\boldsymbol{n}$ and $\widetilde{\boldsymbol{n}}$ be the unit normal vectors to Σ and $\widetilde{\Sigma}$ respectively. Using that $\nabla\Phi = |\nabla\Phi|\boldsymbol{n}$, we have

$$\widetilde{\boldsymbol{n}} = \frac{1}{|\widetilde{\nabla}\widetilde{\Phi}|}\widetilde{\nabla}\widetilde{\Phi} = \frac{1}{|\boldsymbol{A}^{-T}\nabla\Phi|}\boldsymbol{A}^{-T}\nabla\Phi = \frac{|\nabla\Phi|}{|\boldsymbol{A}^{-T}\nabla\Phi|}\boldsymbol{A}^{-T}\boldsymbol{n},$$

which implies that

$$\widetilde{\boldsymbol{n}} = \mu\boldsymbol{A}^{-T}\boldsymbol{n}, \tag{11}$$

where $\mu = |\boldsymbol{A}^{-T}\boldsymbol{n}|^{-1}$ is a scaling factor that ensures that $|\widetilde{\boldsymbol{n}}| = 1$.

Step 2:

We have

$$\boldsymbol{A}^{-1}\boldsymbol{M_0} = \left(\mathbf{Id} - \frac{1}{1+\alpha}\boldsymbol{M_0}\boldsymbol{M_0}^T\right)\boldsymbol{M_0} = \left(1 - \frac{|\boldsymbol{M_0}|^2}{1+\alpha}\right)\boldsymbol{M_0} = \alpha\boldsymbol{M_0}.$$

Starting from [HPN19, Eq. (11)], multiplying by $\boldsymbol{A}^{-1}$ on the left and by $\boldsymbol{A}^{-T}$ on the right, we have

$$c_0^2\boldsymbol{M_0}\boldsymbol{M_0}^T - c_0^2\mathbf{Id} = -c_0^2\boldsymbol{A}^{-1}\boldsymbol{A}^{-T} \iff \boldsymbol{A}^{-1}\boldsymbol{A}^{-T} = \mathbf{Id} - \boldsymbol{M_0}\boldsymbol{M_0}^T. \tag{12}$$

Step 3:

We recall that

$$\widetilde{p}(\widetilde{\boldsymbol{x}},\widetilde{\omega}) = \alpha\exp\left[\frac{i\omega}{\alpha^2 c_0}\boldsymbol{M_0}\cdot\boldsymbol{x}\right]p(\boldsymbol{x},\omega). \tag{13}$$

Using the chain rule, we have

$$\widetilde{\nabla}p = \boldsymbol{A}^{-T}\nabla p, \quad \text{and} \quad \widetilde{\nabla}\left[\alpha\exp\left[\frac{i\omega}{\alpha^2 c_0}\boldsymbol{M_0}\cdot\boldsymbol{x}\right]\right] = \frac{i\omega}{\alpha^2 c_0}\alpha\exp\left[\frac{i\omega}{\alpha^2 c_0}\boldsymbol{M_0}\cdot\boldsymbol{x}\right]\boldsymbol{A}^{-T}\boldsymbol{M_0},$$

and therefore

$$\partial_{\widetilde{\boldsymbol{n}}}\widetilde{p} = \widetilde{\boldsymbol{n}} \cdot \widetilde{\nabla} \widetilde{p}$$

using the definition (13) of $\widetilde{p}$ we have

$$\partial_{\widetilde{\boldsymbol{n}}}\widetilde{p} = \alpha \exp\left[\frac{i\omega}{\alpha^2 c_0}\boldsymbol{M_0}\cdot\boldsymbol{x}\right]\widetilde{\boldsymbol{n}}^T\left(\boldsymbol{A}^{-T}\nabla p + \frac{i\omega}{\alpha^2 c_0} p\boldsymbol{A}^{-T}\boldsymbol{M_0}\right),$$

then, (11) yields

$$\partial_{\widetilde{\boldsymbol{n}}}\widetilde{p} = \alpha \exp\left[\frac{i\omega}{\alpha^2 c_0}\boldsymbol{M_0}\cdot\boldsymbol{x}\right]\mu\boldsymbol{n}^T\boldsymbol{A}^{-1}\left(\boldsymbol{A}^{-T}\nabla p + \frac{i\omega}{\alpha c_0} p\boldsymbol{M_0}\right),$$

using (12) leads to

$$\partial_{\widetilde{\boldsymbol{n}}}\widetilde{p} = \alpha \exp\left[\frac{i\omega}{\alpha^2 c_0}\boldsymbol{M_0}\cdot\boldsymbol{x}\right]\mu\boldsymbol{n}^T\left((\mathbf{Id} - \boldsymbol{M_0}\boldsymbol{M_0}^T)\nabla p + i\frac{\omega}{c_0} p\boldsymbol{M_0}\right),$$

we then divide by c_0^2 and use the definition (5) of $\boldsymbol{\sigma}$ to obtain

$$\partial_{\widetilde{\boldsymbol{n}}}\widetilde{p} = \alpha \exp\left[\frac{i\omega}{\alpha^2 c_0}\boldsymbol{M_0}\cdot\boldsymbol{x}\right]\frac{\mu}{c_0^2}\boldsymbol{n}^T\left(\underbrace{\boldsymbol{K_0}\nabla p + 2i\omega p\boldsymbol{v_0}}_{=-\boldsymbol{\sigma}} - i\omega p\boldsymbol{v_0}\right),$$

finally, the ABC (8b) gives

$$\partial_{\widetilde{\boldsymbol{n}}}\widetilde{p} = \alpha \exp\left[\frac{i\omega}{\alpha^2 c_0}\boldsymbol{M_0}\cdot\boldsymbol{x}\right]\frac{\mu}{c_0^2}\left(\mathcal{Z}p - i\omega p\boldsymbol{v_0}\cdot\boldsymbol{n}\right).$$

We obtain (9b) using (10) and

$$p(\boldsymbol{x},\omega) = \frac{1}{\alpha}\exp\left[\frac{-i\omega}{\alpha^2 c_0}\boldsymbol{M_0}\cdot\boldsymbol{x}\right]\widetilde{p}(\widetilde{\boldsymbol{x}},\widetilde{\omega}).$$

Step 5: The well-posedness of the standard Helmholtz equation with ABCs is a well-known result that can be found *eg.* in [Dup11, Sec. 4.3]. Using Lemma 2, we can see that the convected Helmholtz equation with ABCs inherits the well-posedness of the standard Helmholtz equation through the *Prandtl-Glauert-Lorentz transformation.* ∎

Up to this point, we have worked with the *total flux* $\boldsymbol{\sigma}$ which is a convenient quantity to write a mixed finite formulation of the problem. However when working with continuous primal finite-element methods, it is possible to obtain a formulation whose volumetric part is hermitian, which would lead to an alternative boundary flux [HPN17, HPN19, LMG+20]. This flux is

$$\boldsymbol{g} := -c_0^2\nabla p + (-i\omega p + \boldsymbol{v_0}\cdot\nabla p)\boldsymbol{v_0} = -\boldsymbol{K_0}\nabla p - i\omega p\boldsymbol{v_0}.$$

This alternative flux is related to $\boldsymbol{\sigma}$ by

$$\boldsymbol{g} = \boldsymbol{\sigma} + i\omega p\boldsymbol{v_0},$$

and we can define the following ABC

$$\boldsymbol{g}\cdot\boldsymbol{n} + \mathcal{Z}_{\boldsymbol{g}}p = 0.$$

Corollary 1. *The boundary coefficient $\mathcal{Z}_{\boldsymbol{g}}$ satisfies*

$$\mathcal{Z}_{\boldsymbol{g}}(\boldsymbol{x},\omega) = -|\boldsymbol{A}^{-T}\boldsymbol{n}|c_0^2\widetilde{\mathcal{Z}}(\widetilde{\boldsymbol{x}},\widetilde{\omega}).$$

The construction of the ABCs can also be adapted to the *velocity formulation* of the convected Helmholtz equation (2) which is recalled below for a uniform carrier flow with $\rho_0 \equiv 1$

$$\frac{1}{c_0^2}\left(-i\omega + \boldsymbol{v_0}\cdot\nabla\right)^2\varphi - \operatorname{div}\left(\nabla\varphi\right) = s.$$

For this formulation, the *total flux* can be defined as

$$\boldsymbol{\sigma}_\varphi = \left(\mathbf{Id} - \boldsymbol{M_0}\boldsymbol{M_0}^T\right)\nabla\varphi - 2i\frac{\omega}{c_0}\varphi\boldsymbol{M_0}, \tag{14}$$

and we have

Corollary 2. *If $\mathcal{Z}_\varphi$ satisfies*

$$\mathcal{Z}_\varphi = -|\boldsymbol{A}^{-T}\boldsymbol{n}|\widetilde{\mathcal{Z}} + i\frac{\omega}{c_0}\boldsymbol{M_0}\cdot\boldsymbol{n},$$

then

$$\boldsymbol{\sigma}_\varphi\cdot\boldsymbol{n} + \mathcal{Z}_\varphi\varphi = 0,$$

is an ABC for (14).

2.3. New ABCs for the convected Helmholtz equation in 2D

In this section, we derive the practical values used for the ABCs for the convected Helmholtz equation from Absorbing Boundary Conditions formerly derived for the Helmholtz equation in [BGT82].

2.3.1. Low-order ABCs

In this section, we recall some Absorbing Boundary Conditions on a circle for the Helmholtz equation. The ABCs of this section are specific to the 2D setting, however the extension to 3D is straightforward as the result of Theorem 4 holds for any dimension. Notice that even if Theorem 4 is stated for a uniform flow, the new Absorbing Boundary Conditions can be used in the more general case described by Assumption 3. Indeed as the *Prandtl-Glauert-Lorentz transformation* will only be used to construct the ABCs, the carrier flow only needs to be locally uniform close to the artificial boundary, which we can always assume if the boundary is located far away from the source. The ABCs for the standard Helmholtz equation will define the $\widetilde{\mathcal{Z}}$ operator applied on $\widetilde{\Sigma}$. The value of $\mathcal{Z}$ will then be obtained using the transformation of the time-harmonic solutions described in Lemma 1 and the transformation of the boundary coefficients described in Theorem 4.

We will consider the low-order Bayliss-Guntzburger-Turkel Absorbing Boundary Conditions, described in [BGT82], in the Lorentz variable.

We assume that the artificial boundary in Lorentz coordinates $\widetilde{\Sigma}$ is a circle of radius R.

Proposition 1. *Low-order ABCs for the convected Helmholtz equation are:*

- *ABC of order 0:*

$$\boldsymbol{\sigma}\cdot\boldsymbol{n}+\mathcal{Z}p=0,\quad \textit{with } \mathcal{Z}:=i\left(\frac{c_0}{\alpha}|\boldsymbol{A}^{-T}\boldsymbol{n}|+\boldsymbol{v_0}\cdot\boldsymbol{n}\right)\omega, \tag{ABC0}$$

- *ABC of order 1:*

$$\boldsymbol{\sigma}\cdot\boldsymbol{n}+\mathcal{Z}p=0,\quad \textit{with } \mathcal{Z}:=\frac{-c_0^2}{2R}|\boldsymbol{A}^{-T}\boldsymbol{n}|+i\left(\frac{c_0}{\alpha}|\boldsymbol{A}^{-T}\boldsymbol{n}|+\boldsymbol{v_0}\cdot\boldsymbol{n}\right)\omega. \tag{ABC1}$$

Proof. *ABC of order 0.* According to [BGT82], the zeroth order ABC the standard Helmholtz equation reads

$$\left(\partial_{\widetilde{\boldsymbol{n}}}-i\frac{\widetilde{\omega}}{c_0}\right)\widetilde{p}=0.$$

The boundary coefficients are therefore defined by

$$\widetilde{\mathcal{Z}}:=-i\frac{\widetilde{\omega}}{c_0}\quad\text{and}\quad \mathcal{Z}:=i\left(\frac{c_0}{\alpha}|\boldsymbol{A}^{-T}\boldsymbol{n}|+\boldsymbol{v_0}\cdot\boldsymbol{n}\right)\omega.$$

ABC of order 1. According to [BGT82], the first order ABC for the standard Helmholtz equation reads

$$\left(\partial_{\widetilde{\boldsymbol{n}}}-i\frac{\widetilde{\omega}}{c_0}+\frac{1}{2R}\right)\widetilde{p}=0.$$

The boundary coefficients are therefore defined by

$$\widetilde{\mathcal{Z}}:=-i\frac{\widetilde{\omega}}{c_0}+\frac{1}{2R}\quad\text{and}\quad \mathcal{Z}:=\frac{-c_0^2}{2R}|\boldsymbol{A}^{-T}\boldsymbol{n}|+i\left(\frac{c_0}{\alpha}|\boldsymbol{A}^{-T}\boldsymbol{n}|+\boldsymbol{v_0}\cdot\boldsymbol{n}\right)\omega.$$

Remark 2.6. In [BT82], the author derived far-field boundary conditions for the steady-state Euler's equations by applying a change of coordinates which corresponds to the *Prandtl-Glauert-Lorentz transformation*. If they had used their idea to obtain an ABC for the convected Helmholtz equation, this would have led to (ABC1).

It is interesting to dispose of another ABC constructed by adopting another point of view. For that purpose, we will derive an ABC that selects outgoing plane waves that are locally orthogonal to the artificial boundary Σ.

Proposition 2. *The ABC that selects the outgoing plane waves that are locally orthogonal to the boundary is*

$$\boldsymbol{\sigma}\cdot\boldsymbol{n}+\mathcal{Z}p=0,\quad \textit{with } \mathcal{Z}:=i(c_0+\boldsymbol{v_0}\cdot\boldsymbol{n})\omega. \tag{ABC-PW}$$

PROOF. We begin by computing the plane waves for the convected Helmholtz equation (1). We write p as

$$p_{PW} = p_0 e^{i\boldsymbol{\kappa}\cdot\boldsymbol{x}}$$

where $p_0 \in \mathbb{C}$ and where $\boldsymbol{\kappa}$ is the wave vector. We can rewrite (1) as

$$p_0 \left[-\omega^2 + 2\omega \boldsymbol{v_0}\cdot\boldsymbol{\kappa} + \boldsymbol{\kappa}^T \boldsymbol{K_0}\boldsymbol{\kappa}\right] = 0,$$

and therefore

$$-\rho_0\omega^2 + 2\omega\rho_0 \boldsymbol{v_0}\cdot\boldsymbol{\kappa} + \rho_0 c_0^2 |\boldsymbol{\kappa}|^2 - \rho_0(\boldsymbol{v_0}\cdot\boldsymbol{\kappa})^2 = 0. \tag{15}$$

As we only have one equation for two unknowns, we make the following assumptions

$$\begin{aligned} \boldsymbol{\kappa} &:= \kappa \begin{bmatrix}\cos\theta \\ \sin\theta\end{bmatrix}, && \text{where } \theta \in [0, 2\pi) \text{ is assumed to be known,} \\ \boldsymbol{v_0} &:= Mc_0 \begin{bmatrix}\cos\theta_0 \\ \sin\theta_0\end{bmatrix}, && \text{where } \theta_0 \in [0, 2\pi). \end{aligned}$$

With those assumptions, (15) becomes

$$-\omega^2 + 2\omega\kappa M c_0 \left(\cos\theta_0\cos\theta + \sin\theta_0\sin\theta\right) + c_0^2\kappa^2 - M^2 c_0^2 \kappa^2 \left(\cos\theta_0\cos\theta + \sin\theta_0\sin\theta\right)^2 = 0,$$

or equivalently

$$-\omega^2 + 2\omega\kappa M c_0 \cos(\theta - \theta_0) + c_0^2\kappa^2 \left(1 - M^2\cos^2(\theta - \theta_0)\right) = 0.$$

Solving this last equation for κ leads to the two following solutions

$$\kappa_- = \frac{-\omega}{c_0(1 - M\cos(\theta - \theta_0))} \quad \text{and} \quad \kappa_+ = \frac{\omega}{c_0(1 + M\cos(\theta - \theta_0))}.$$

Notice that $\boldsymbol{\kappa}$ can be rewritten as

$$\boldsymbol{\kappa} = \frac{\kappa_\pm}{Mc_0}\left(\cos(\theta - \theta_0)\boldsymbol{v_0} + \sin(\theta - \theta_0)\boldsymbol{v_0^\perp}\right).$$

The plane-wave solutions of (4) are therefore

$$p_{PW} = p_0 e^{i\boldsymbol{\kappa}_\pm\cdot\boldsymbol{x}}, \quad \text{with} \quad \kappa_\pm = \frac{\pm\omega}{c_0(1 \pm M\cos(\theta - \theta_0))},$$

and the total flux $\boldsymbol{\sigma}_{PW}$ therefore satisfies

$$\boldsymbol{\sigma}_{PW} = -i\frac{c_0\kappa_\pm}{M}\left((1 - M^2)\cos(\theta - \theta_0)\boldsymbol{v_0} + \sin(\theta - \theta_0)\boldsymbol{v_0^\perp}\right) p_0 e^{i\boldsymbol{\kappa}\cdot\boldsymbol{x}}.$$

As we want to select plane-waves that are locally orthogonal to the artificial boundary Σ, we have

$$\frac{\boldsymbol{\kappa}_\pm}{|\boldsymbol{\kappa}_\pm|} = \boldsymbol{n} = \begin{bmatrix}\cos\theta \\ \sin\theta\end{bmatrix},$$

leading to

$$\boldsymbol{v_0}\cdot\boldsymbol{n} = Mc_0\cos(\theta-\theta_0), \quad \text{and} \quad \boldsymbol{v_0}^{\perp}\cdot\boldsymbol{n} = Mc_0\sin(\theta-\theta_0).$$

We then have

$$\boldsymbol{\sigma}\cdot\boldsymbol{n} = -i\omega c_0\left(1\pm M\cos(\theta-\theta_0)\right)p = -i\omega\left(c_0\pm\boldsymbol{v_0}\cdot\boldsymbol{n}\right)p.$$

We can now define the boundary coefficients $\mathcal{Z}$ as

$$\mathcal{Z} = \frac{-\boldsymbol{\sigma}_{PW}\cdot\boldsymbol{n}}{p_{PW}} = i\omega(c_0+\boldsymbol{v_0}\cdot\boldsymbol{n}),$$

which leads to what we call (ABC-PW)

$$\boldsymbol{\sigma}\cdot\boldsymbol{n} + i\omega(c_0+\boldsymbol{v_0}\cdot\boldsymbol{n})p = 0.$$

We have chosen the ABC with the + sign as a consequence of the convention $e^{-i\omega t}$ that we use for time-harmonic solutions .

Remark 2.7. The two ABCs (ABC0) and (ABC-PW) are different. Indeed for the standard Helmholtz equation, the zeroth order Bayliss-Guntzburger-Turkel ABC is exact for plane waves that are locally orthogonal to the boundary. This property is not preserved when we convert the Helmholtz equation into its convected counterpart via the *Prandtl-Glauert-Lorentz transformation*. To illustrate why this fact, let us consider the simple case where $\boldsymbol{v_0} = Mc_0\boldsymbol{e}_x$. In this case, a plane wave solution to the convected Helmholtz equation (1) with incident angle θ is given by

$$p(\boldsymbol{x},\omega) = \exp\left[\frac{i\omega}{c_0(1+M\cos\theta)}(x\cos\theta+y\sin\theta)\right],$$

using Lemma 1, we have

$$\widetilde{p}(\widetilde{\boldsymbol{x}},\widetilde{\omega}) = \alpha\exp\left[\frac{i\omega}{\alpha^2 c_0}Mx\right]\exp\left[\frac{i\omega}{c_0(1+M\cos\theta)}(x\cos\theta+y\sin\theta)\right],$$

which leads to

$$\widetilde{p}(\widetilde{\boldsymbol{x}},\widetilde{\omega}) = \alpha\exp\left[\frac{i\omega}{\alpha c_0}\left(\frac{M}{\alpha}+\frac{\alpha\cos\theta}{1+M\cos\theta}\right)x + \frac{i\omega}{\alpha c_0}\frac{\alpha\cos\theta}{1+M\cos\theta}y\right].$$

Using that $\boldsymbol{x} = \boldsymbol{A}^{-1}\widetilde{\boldsymbol{x}}$, we get $x = \alpha\widetilde{x}$ and $y = \widetilde{y}$, and we finally obtain that

$$\widetilde{p}(\widetilde{\boldsymbol{x}},\widetilde{\omega}) = \alpha\exp\left[\frac{i\omega}{\alpha c_0}\left(\frac{M+\cos\theta}{1+M\cos\theta}\widetilde{x}+\frac{\alpha\sin\theta}{1+M\cos\theta}\widetilde{y}\right)\right] = \alpha\exp\left[\frac{i\widetilde{\omega}}{c_0}\left(\cos\widetilde{\theta}\widetilde{x}+\sin\widetilde{\theta}\widetilde{y}\right)\right],$$

where

$$\widetilde{\theta} = \arctan\left(\frac{\alpha\sin\theta}{M+\cos\theta}\right).$$

When $M\neq 0$, we have $\widetilde{\theta}\neq\theta$, and we can therefore conclude that the incident angle of a plane wave changes under the *Prandtl-Glauert-Lorentz transformation*. As (ABC0) is derived for a plane wave that is locally orthogonal to the boundary in PGL coordinates, the resulting plane wave is not normal to the boundary in physical coordinates. This explains the difference with (ABC-PW). This is natural since the acoustic intensity vector is not orthogonal to the wavefront in the presence of a flow.

2.3.2. Extension to higher order ABCs

In this section, we will illustrate how the *Prandtl-Glauert-Lorentz transformation* can be used to derived higher-order ABCs, even if those ABCs do not naturally fit in the framework of DG methods. For the sake of simplicity, we only consider the case $\boldsymbol{v_0} = Mc_0\boldsymbol{e}_y$. The general case can then be obtained by rotation. We introduce the elliptical coordinates (μ, ν) defined by

$$x = c\cosh\mu\cos\nu, \quad y = c\sinh\mu\sin\nu,$$

and the artificial boundary Σ is described by setting a constant value for μ. On the other hand, the artificial boundary in PGL-coordinates is represented as

$$\widetilde{x} = R\cos\widetilde{\theta}, \quad \widetilde{y} = R\sin\widetilde{\theta},$$

for some constant R. Using that $\boldsymbol{x} = \boldsymbol{A}^{-1}\widetilde{\boldsymbol{x}}$, we have

$$c\cosh\mu = R, \quad c\sinh\mu = R\alpha, \quad \nu = \widetilde{\theta}.$$

It is now straightforward to obtain a second-order ABC for the convected Helmholtz equation. For the standard Helmholtz equation, a complete second-order ABC on a circular boundary is given by

$$\partial_{\widetilde{\boldsymbol{n}}}\widetilde{p} + B\widetilde{p} + D\partial^2_{\widetilde{\theta}\widetilde{\theta}}\widetilde{p} = 0,$$

where

$$B := -\frac{i\omega}{c_0} + \frac{1}{2R} + \frac{1}{8i\frac{\omega}{c_0}R(1+\frac{ic_0}{\omega R})},$$
$$D := \frac{1}{2\frac{i\omega}{c_0}R(1+\frac{ic_0}{\omega R})}\frac{1}{R^2},$$

see [ABB99, Eq. (28)]. We can therefore define $\widetilde{\mathcal{Z}}$ as

$$\widetilde{\mathcal{Z}} := B + D\partial^2_{\widetilde{\theta}\widetilde{\theta}},$$

using Theorem 4 we finally obtain the following ABC for the convected Helmholtz equation

$$\boldsymbol{\sigma}\cdot\boldsymbol{n} + \mathcal{Z}p = 0,$$

where

$$\mathcal{Z}p(\boldsymbol{x},\omega) = -c_0^2|\boldsymbol{A}^{-T}\boldsymbol{n}|\Big[Bp + D\Big(\partial^2_{\nu\nu}p + \frac{2i\omega Mc}{\alpha^2c_0}\sinh\mu\cos\nu\partial_\nu p + \frac{i\omega Mc}{\alpha^2c_0}\sinh\mu\left(\frac{2i\omega Mc}{\alpha^2c_0}\sinh\mu\cos^2\nu + i\sin\nu\right)p\Big) - \frac{i\omega M}{\alpha c_0}\sin\nu p\Big].$$

This resulting ABC is different from the ones derived in [HHT03, BGH10], as they take the elliptical shape of the boundary into account while the conditions in [HHT03, BGH10] have been derived for flat boundaries only. This ABC will not be considered in this paper because its implementation into the underlying HDG formulation is a challenging issue due to the discretization of the first and second order surface derivatives. This question will be addressed in a further work.

3. Numerical experiments

The numerical experiments of this section have been performed using the HDG-$\boldsymbol{\sigma}$ method of [BRT21] which has been implemented in the open-source software package `hawen`, see [Fau21].

We solve the following *first-order in space and second-order in frequency* formulation:

$$\begin{aligned} \boldsymbol{\sigma} + \boldsymbol{K_0}\nabla p + 2i\omega p \boldsymbol{v_0} &= 0, \\ -\omega^2 p + \operatorname{div}(\boldsymbol{\sigma}) &= s. \end{aligned}$$

As the *total flux* $\boldsymbol{\sigma}$ is an unknown of the method, it is very natural to work with the ABCs of Proposition 1. The experiments that are presented in this paper have been carried out with a nodal basis with interpolation degree $k = 5$.

3.1. Experiments with a uniform flow

We consider a point-source in a uniform flow

$$\boldsymbol{M_0} := M \begin{bmatrix} \cos\theta_0 \\ \sin\theta_0 \end{bmatrix}, \quad s = \delta_{\mathbf{0}}, \quad c_0 = 1, \quad \omega = 6\pi.$$

Following [MBAG21], we define the number of degrees of freedom per shortest wavelength as

$$d_\lambda := \frac{2\pi k}{\omega h}(1 - M).$$

In practice we choose $h = 0.05$, and for the highest Mach number $M = 0.8$ we have $d_\lambda \simeq 6.7$, which is similar to the parameters used in [MBAG21]. The Dirac source-term located at $\boldsymbol{x}_0$ is discretized as

$$\int_K \delta_{\boldsymbol{x}_0} \Phi_i^K \mathrm{d}\boldsymbol{x} = \Phi_i^K(\boldsymbol{x}_0),$$

on element K and for all basis functions Φ_i^K. To handle the singularity due to this term, the mesh is refined around $\boldsymbol{x}_0$ by halving h. In the numerical experiments presented below, we have taken $\boldsymbol{x}_0 = \mathbf{0}$.

A reference solution of the Helmholtz equation reads:

$$\widetilde{p}_{\mathrm{ref}}(\widetilde{\boldsymbol{x}}, \widetilde{\omega}) = \frac{i}{4} H_0^{(1)}(\widetilde{\omega}\widetilde{r}),$$

and from Lemma 1, we deduce that a reference solution to the convected Helmholtz equation is:

$$p_{\mathrm{ref}}(\boldsymbol{x}, \omega) = \frac{i}{4\alpha} H_0^{(1)}\left(\frac{\omega}{\alpha}|\boldsymbol{A}\boldsymbol{x}|\right) \exp\left(-\frac{i\omega}{\alpha^2 c_0}\boldsymbol{M_0}\cdot\boldsymbol{x}\right). \tag{16}$$

To begin with, we will use $\theta_0 = \frac{\pi}{4}$ as it leads to a circular artificial boundary in both physical and PGL coordinates. Numerical experiments illustrating the influence of the flow angle θ_0 will be given in the end of this section.

As the parameter R, which represents the size of the domain in PGL coordinates, is not really meaningful, we introduce the *Helmholtz number*

$$\mathrm{He} := \frac{\omega \alpha R}{2\pi(1+M)},$$

which describes the number of largest wavelengths inside the domain. In the above formula, $\omega/(2\pi(1+M))$ denotes the wavenumber of the waves propagating with the flow and, αR is the size of the domain in physical coordinates (as $|\boldsymbol{A}\boldsymbol{x}| \simeq |\boldsymbol{x}|/\alpha$).

3.1.1. Validation of the ABCs

For a numerical solution p_h, we define the relative error as

$$\mathcal{E}_{\mathcal{O}} := \sqrt{\frac{\sum_{K,i} |p_h - p_{\mathrm{ref}}|^2(\boldsymbol{x}_i^K)}{\sum_{K,i} |p_{\mathrm{ref}}|^2(\boldsymbol{x}_i^K)}},$$

where $(\boldsymbol{x}_i^K)_i$ are the degrees of freedom in element $K \in \mathcal{T}_h$. The triangulation $\mathcal{T}_h$ is composed of triangles K. As the solution p_{ref} is singular at $\boldsymbol{x} = \boldsymbol{0}$, the error will be computed on $\mathcal{O} \backslash B(\boldsymbol{0}, \rho)$ where $B(\boldsymbol{0}, \rho)$ is the open ball centered on $\boldsymbol{x} = \boldsymbol{0}$ with radius $\rho = 2h$.

Low Mach number. The relative error $\mathcal{E}_{\mathcal{O}}$ for various values of He is given in Table 1 for a low Mach number $M = 0.4$. In this case, we can see that the three ABCs perform well, with a clear advantage in favor of the two PGL-based ABCs ((ABC0) and (ABC1)). As expected, (ABC1) performs better than (ABC0) and for $M = 0.4$, we can see that a relative error of $\sim 0.1\%$ is obtained even with $\mathrm{He} = 1$.

R	He	(ABC0)	(ABC1)	(ABC-PW)
0.5	1	3.47%	0.12%	4.8%
1.0	2	1.51%	0.13%	3.72%
1.5	3	0.89%	0.12%	3.33%
2.0	4	0.70%	0.12%	3.12%

Table 1: Relative error $\mathcal{E}_{\mathcal{O}}$ in the domain for $M = 0.4$

Intermediate Mach number. In Table 2, the relative error $\mathcal{E}_{\mathcal{O}}$ is computed for several values of R for $M = 0.6$. In this case (ABC-PW) performs badly, leading to an error level of $\sim 10\%$, whereas the PGL-based ABCs give good numerical results with an error level of $\sim 1\%$. This is also illustrated in Figure 3. Once again (ABC1) performs better than (ABC0). Indeed (ABC1) leads to an error level below 1% even for very small values of He whereas a larger He is required to obtain a similar error level with (ABC0).

R	He	(ABC0)	(ABC1)	(ABC-PW)
0.5	0.75	2.14%	0.67%	8.3%
1.0	1.5	1.21%	0.62%	7.31%
1.5	2.25	0.98%	0.66%	8.02%
2.0	3.0	0.83%	0.64%	7.1%

Table 2: Relative error $\mathcal{E}_{\mathcal{O}}$ in the domain for $M = 0.6$

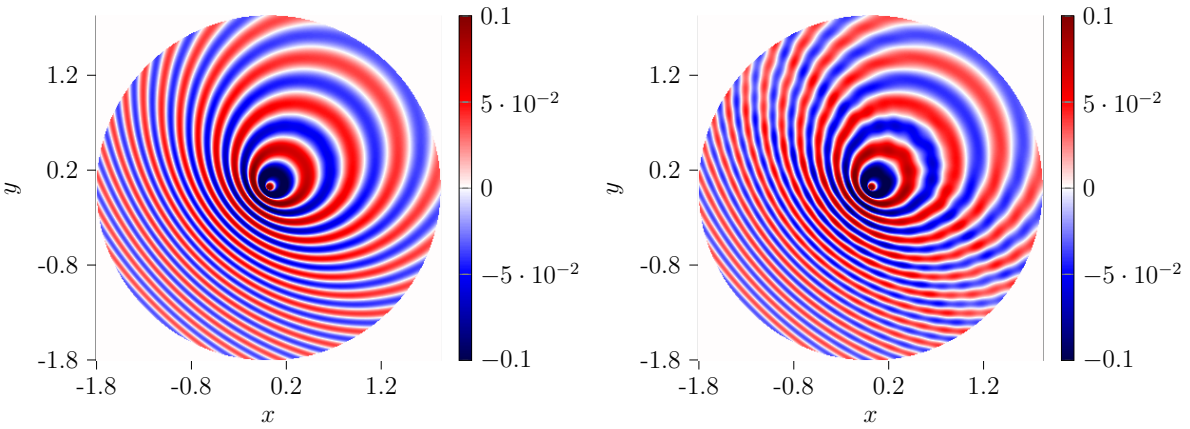

(a) ABC1 (b) ABC-PW

Figure 3: Comparison between two ABCs for $M = 0.6$ and $\mathrm{He} = 3$

To understand the distribution of the error in the domain, we also consider the local error

$$\mathcal{E}_{\mathrm{loc}}(\boldsymbol{x}) := |p_h - p_{\mathrm{ref}}|(\boldsymbol{x}).$$

In Figure 4, the local error is plotted for (ABC1) and (ABC-PW) for $M = 0.6$ and $R = 2$. For (ABC-PW) there is a clear pattern: the ABC performs better in the top-right and bottom-left parts of the domain. This can be understood as this ABC is constructed to select outgoing plane-waves that are locally orthogonal to the boundary. By looking at Figure 3, we can see that p is almost orthogonal to the boundary in the top-right and bottom-left parts of the domain where (ABC-PW) performs well. However due to the presence of convection, p is clearly not orthogonal to the boundary in the top-left and bottom-right parts of the domain, where ABC-PW exhibits its worst behavior. For (ABC1) the error seems better distributed inside the domain, and we can clearly see that the error level is one order of magnitude smaller than the error level of (ABC-PW).

To further illustrate this idea, we also consider the *local error* on the artificial boundary Σ

$$\mathcal{E}_{\Sigma} := |(p_h - p_{\mathrm{ref}})|_{\Sigma}| \,.$$

This error is depicted in Figure 5 for (ABC1) and (ABC-PW). For (ABC-PW), the same effect as in Figure 4 can be seen. For (ABC1) however, we notice that most of the error

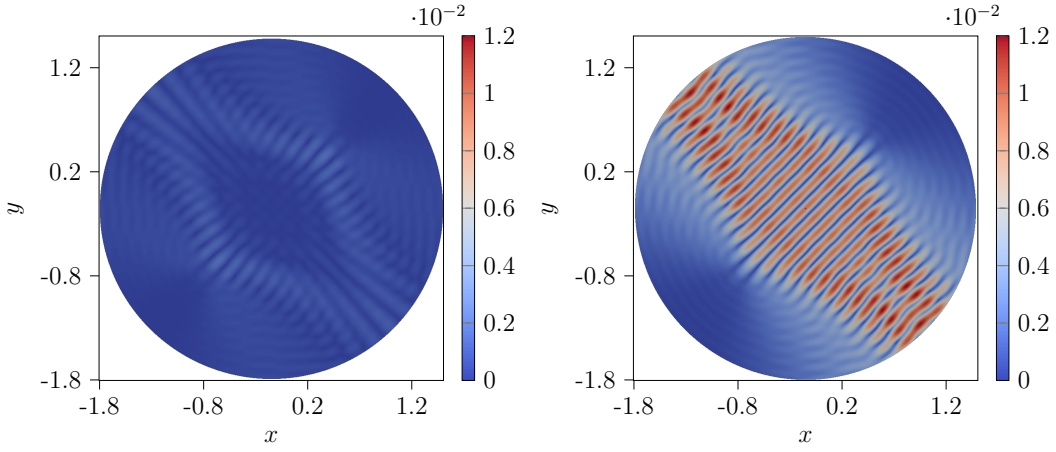

(a) ABC1 (b) ABC-PW

Figure 4: Local error $\mathcal{E}_{\text{loc}}$ in the domain for $M = 0.6$ and $\text{He} = 3$

is located in bottom part of the domain. The effects of the flow angle θ_0 on this error distribution will be discussed in Table 4 at the end of this section. We would like to point out that the error levels for (ABC1) are one order of magnitude lower than those of (ABC-PW) as expected.

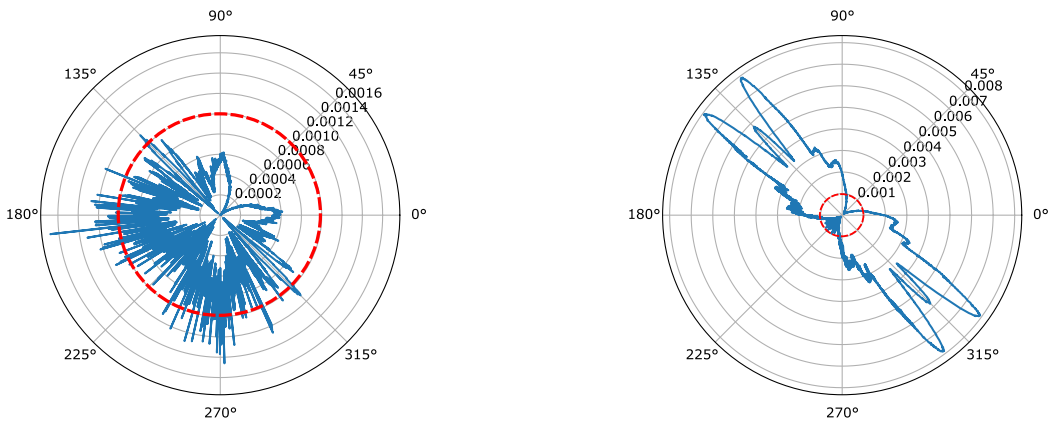

(a) ABC1 (b) ABC-PW

Figure 5: Local error $\mathcal{E}_\Sigma$ on Σ for $M = 0.6$ and $\text{He} = 3$. The red circle is the same on the two pictures.

Large Mach number. For a large Mach number, the use of the PGL-based ABCs leads to a higher error. It therefore seems natural to consider larger domain, but as it can be seen in Table 3, even for $\text{He} = 10$ the error does not get below 1.84% with (ABC1). This level of error occurs even if the Helmholtz number He is higher than in the cases of low and intermediate Mach numbers. It also seems that in this case, using (ABC1) instead of

(ABC0) does not improve the quality of the solution. In FIGURE 6, the numerical solutions p_h obtained with (ABC1) and (ABC-PW) are depicted.

R	He	(ABC0)	(ABC1)	(ABC-PW)
3	3	2.41%	2.39%	15.29%
10	10	1.85%	1.84%	14.87%

Table 3: Relative error $\mathcal{E}_{\mathcal{O}}$ in the domain for $M = 0.8$

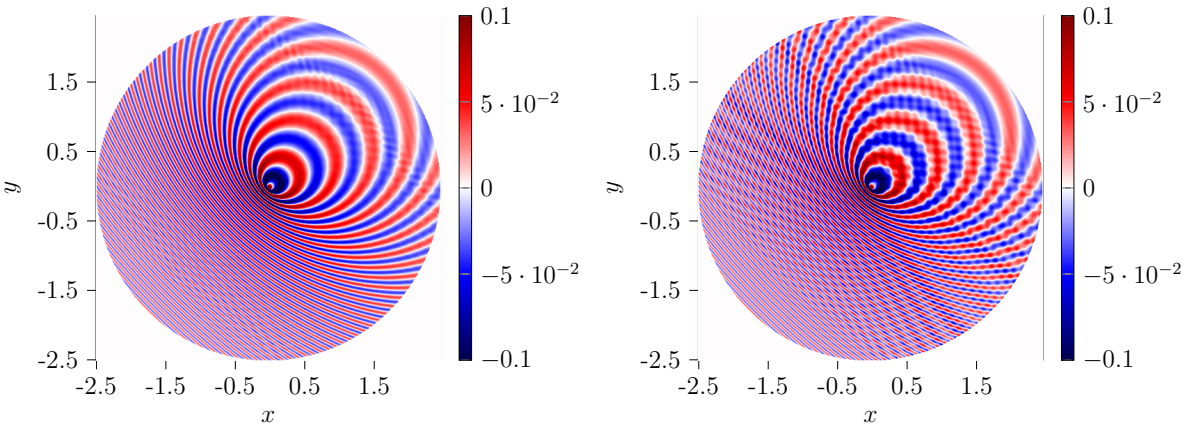

(a) ABC1 (b) ABC-PW

Figure 6: Comparison between two ABCs for $M = 0.8$ with $R = 3$

In FIGURE 7 we have depicted the numerical solution p_h and the local error $\mathcal{E}_{\text{loc}}$ for ABC1 with He = 10. Even if the relative error $\mathcal{E}_{\mathcal{O}}$ is of 1.84%, by looking at the plot of $\mathcal{E}_{\text{loc}}$ it seems possible to trust the solution far enough from the artificial boundary. A domain of this size satisfies the convergence criterion $R > (1 - M^2)^{-1}$ suggested in [HHT03], as the error level is still quite important we can probably conclude that the difficulties in dealing with high Mach numbers are an intrinsic feature of low-order ABCs. A similar conclusion can be drawn from [HHT03, FIG. 5].

To further illustrate the influence of the Mach number, the relative error $\mathcal{E}_{\mathcal{O}}$ has been plotted as a function of M with fixed Helmholtz number He = 3 in FIGURE 8. In this figure, we can see that the error stays below 1% for Mach numbers up to 0.6. Starting at $M = 0.7$, the errors become quite large and more advanced domain truncation techniques should be preferred, as for instance the use of high-order ABCs.

Finally we would like to point out that considering a larger domain leads to a much more expensive problem from a computational point of view. The numerical experiments were run on a `miriel` node of the `plafrim` cluster[1] equipped with 2 dodeca-core Haswell Intel

[1]See `https://www.plafrim.fr`.

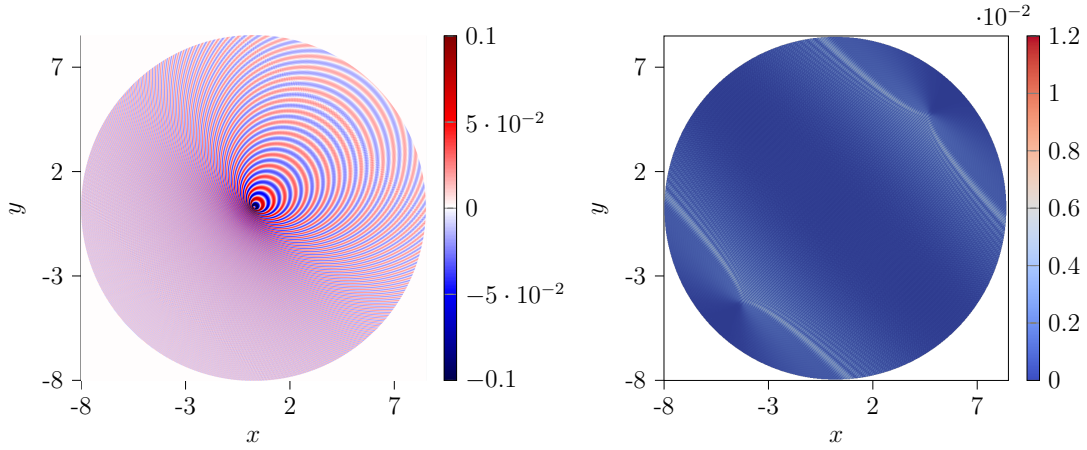

(a) Numerical solution p_h (b) $\mathcal{E}_{\text{loc}}$

Figure 7: Results and error for ABC1 with $M = 0.8$ and $\text{He} = 10$

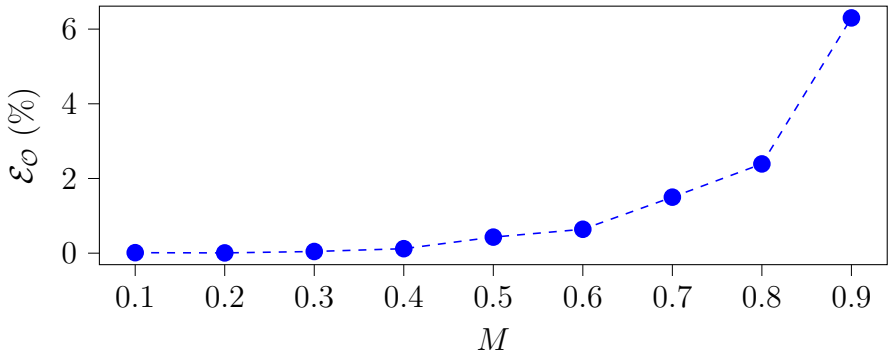

Figure 8: Relative error $\mathcal{E}_{\mathcal{O}}$ (in %) as a function of the Mach number M for a fixed Helmholtz number $\text{He} = 3$.

Xeon E5-2680 v3 with a clock rate of 2.5 GHz and 128 Go of memory. The case of the small domain with $\text{He} = 3$ ran in 1min, whereas for the test with $\text{He} = 10$, it took 1h15min to run.

Comparison with PMLs. For the convected Helmholtz equation, usual PMLs are known to be unstable. In [BDL04] stable PMLs for the convected Helmholtz equation were derived, but only for propagation in a waveguide. This work was extended to arbitrary geometries in [MBAG21], this formulation is also based on the *Prandtl-Glauert-Lorentz transformation*. For high Mach numbers, the so-called Lorentz PMLs of [MBAG21] seem to perform better than the ABCs of this paper. Indeed, the authors were able to obtain an error level of 1.2% using a smaller domain for $M = 0.8$. However this formulation seems difficult to implement in the context of HDG methods and, as stated in [MBAG21], their efficiency for non-uniform flows remains unclear. However, as it will be illustrated in Subsection 3.2, the PGL-based ABCs can be used for cases where the background flow changes inside the domain.

Comparison with other low-order ABCs. In [Gab03, Chap. 3] and [Bér08, Chap. 5], ABCs for Galbrun's equation are studied. Galbrun's equation is an aeroacoustic model which is more realistic than the convected Helmholtz equation as it allows for more general background flows. However the ABCs derived in those dissertations were only illustrated with uniform flows for which the two models are equivalent. This is why as the reference solution used in [Bér08, p. 129 - last equation] is the same as the one we described in (16). Even if various conditions are described, the best performing one is somewhat similar to (ABC-PW), and the authors only obtained an error level of 4.5% for $M = 0.3$ and $\omega = 6\pi$. It seems interesting to extend the PGL-based ABCs to Galbrun's equation. This generalization is difficult, except in the case of a potential flow, where Galbrun's equation reduces to the convected Helmholtz equation.

Comparison with high-order ABCs. In [HHT03], high-order ABCs were constructed for the time-domain convective wave equation. Obviously the comparison is not really relevant but for $M = 0.4$, we see on Figures 3 and 4 of this paper that the error level of (ABC1) is lower than the error level of ABC with $l = 1$ and similar to the error level of ABC with $l = 5$ in [HHT03]. For $M = 0.8$, we can see on FIG. 5 that the low-order ABC of [HHT03] has a similar or higher error level than (ABC1), however the higher-order ABCs lead to better numerical results. This observation turns in favor of using high-order conditions for high Mach numbers.

3.1.2. Influence of the flow angle

In this section, we focus on the influence of the flow angle θ_0 on the performance of the ABCs. In Table 4 the errors obtained when using (ABC1) are given for various values of θ_0. We can clearly see that $\mathcal{E}_\mathcal{O}$ is smaller when the flow is aligned with one of the axis (for $\theta_0 = 0$ or $\theta_0 = \pi/2$). This can be understood as the change of spatial coordinates $\boldsymbol{A}^{-1}$, which is used to construct the ABCs, is contracting: the domain is smaller in physical coordinates than in PGL ones. When $\theta_0 = 0$ or $\pi/2$, this contraction only occurs in one direction, whereas it occurs in both directions for the other values of θ_0. The error is therefore smaller when the flow is aligned with one of the axis. The maximal error appears to be achieved for $\theta_0 = \pi/4$ which is the angle with the highest contraction, as both directions are contracted in the same way.

Flow angle θ_0	Error $\mathcal{E}_\mathcal{O}$
0	$1.32 \cdot 10^{-3}\%$
$\pi/3$	0.29%
$\pi/4$	0.51%
$\pi/6$	0.30%
$\pi/2$	$1.31 \cdot 10^{-3}\%$

Table 4: Domain error $\mathcal{E}_\mathcal{O}$ for $M = 0.6$ with (ABC1) and $R = 2.5$ corresponding to $\mathrm{He} = 3.75$

As the error seems minimal for a flow aligned with one of the axis, performing a rotation

should therefore be considered before using those ABCs. However as the relative error stays below 1%, results obtained for other values of θ_0 are still acceptable.

Some of the cases of TABLE 4 are depicted in FIGURE 9. On those figures, the elliptical shape of the domain can clearly be seen when $\theta_0 \neq \pi/4$, as well as the contraction effect due to the change of coordinates.

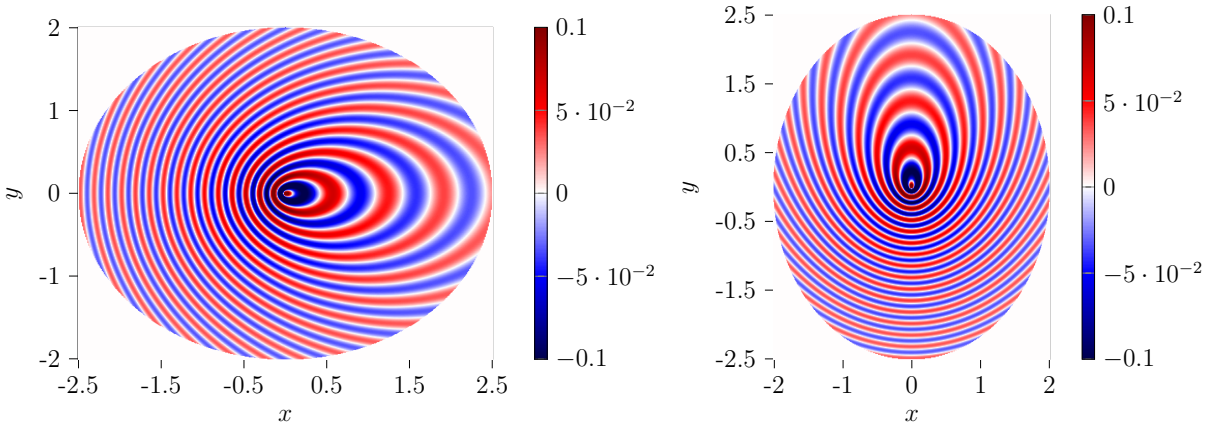

(a) $\theta_0 = 0$ (b) $\theta_0 = \pi/2$

Figure 9: Numerical examples for various values of θ_0 with $M = 0.6$ and ABC1

3.1.3. Experiments with multiple sources

To illustrate the ability of the ABCs to handle more complex cases, we consider multiple point-sources in a uniform flow. For the numerical simulations, we consider the following parameters associated to a large Helmholtz number He $\simeq 9.4$, which corresponds to

$$M = 0.6, \quad \theta_0 = \frac{\pi}{4}, \quad \omega = 12.5\pi, \quad R = 2. \tag{17}$$

The sources will be located at $(\pm 0.1, \pm 0.1)$ for the case with two point-sources and at $(\pm 0.1, \pm 0.1)$ and $(\pm 0.1, \mp 0.1)$ for the case with four point-sources. In those cases, an analytic solution can be obtained by superposition of the analytic solution (16) for one point-source. To evaluate the error, a ball of radius $\rho = 4h$ is excluded to remove the points where the solution is singular.

In FIGURE 10 the results obtained with the above parameters and (ABC1) are depicted. We can clearly see the interference patterns between the sources as well as changes in the apparent frequency due to the Doppler effect. Those physical phenomena are well-reproduced without any visible spurious effect of the ABC. For the case with two point-sources, we obtained an error level of $\mathcal{E}_{\mathcal{O}} = 1.003\%$ and $\mathcal{E}_{\Sigma}^{\text{rel}} = 3\%$, where

$$\mathcal{E}_{\Sigma}^{\text{rel}} = \sqrt{\frac{\sum_{K,i} |p_h - p_{\text{ref}}|^2(\boldsymbol{x}_i^{K\cap\Sigma})}{\sum_{K,i} |p_{\text{ref}}|^2(\boldsymbol{x}_i^{K\cap\Sigma})}},$$

is the relative error on the boundary. In [AH01], the authors used infinite elements for the convected elements. The parameters described in (17) are similar to the case depicted in [AH01, Fig. 5 & 6, case b) with $kD = 10$]. The performances of their numerical method are better than ours when Mesh A is used as they obtain an error level of $\mathcal{E}_\Sigma^{\text{rel}} = 0.2\%$[2]. If Mesh B is used, the infinite elements and the PGL-based ABCs exhibit similar performances. It is worth noting that in [AH01], the error is computed when a flux issued from an analytic solution is prescribed at the beginning of the infinite elements, and the coupling between infinite elements and a numerical method in the interior domain is not done. The implementation of this coupling would involve an approximation of the Dirichlet-to-Neumann operator at the interface between infinite and finite elements, which should introduce some additional error. Moreover, it is also not clear whether and how this coupling could be adapted to the framework of HDG methods.

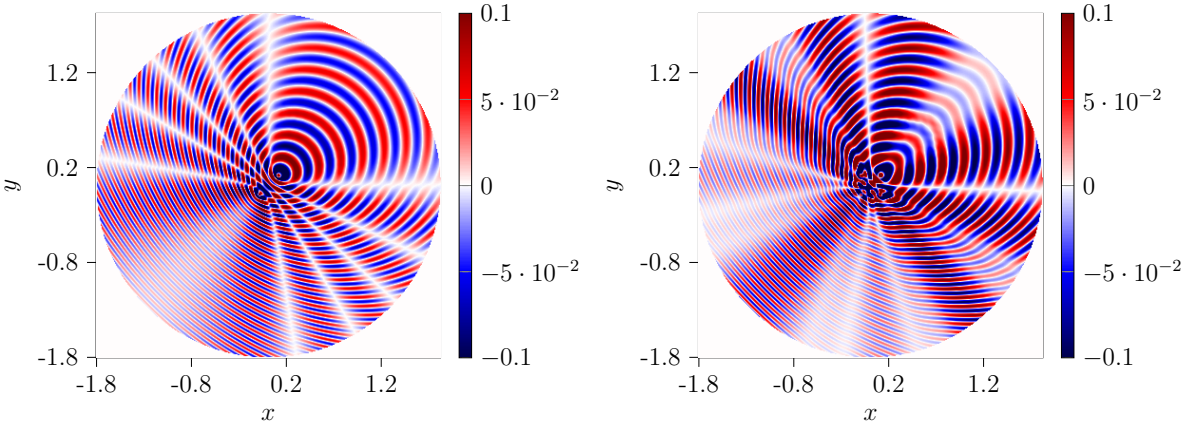

(a) Two point-sources

(b) Four point-sources

Figure 10: Interferences between multiple point-sources for $M = 0.6$ with ABC1

3.2. Experiments with a potential flow

In this section, we give illustrative examples where the PGL-based ABCs are used with a non-uniform flow. As the convected Helmholtz equation is only valid for potential flows, we focus on the case of a potential flow around a circular obstacle.

The ABCs of this paper are constructed for an artificial boundary Σ centered on the source. The expression for the potential flow should therefore be translated as it is usually written for a circular obstacle located at $(0, 0)$.

We assume that the obstacle has a radius R_C and its center is located at $\boldsymbol{x}_C = (x_C, y_C)$. For a point $\boldsymbol{x} = (x, y)$, we define the translated polar coordinates around $\boldsymbol{x}_C$ by

$$r := |\boldsymbol{x} - \boldsymbol{x}_C|, \quad \text{and} \quad \theta := \arctan\left(\frac{y - y_C}{x - x_C}\right).$$

[2]We have multiplied the error by two, as the authors consider a symmetric domain and only compute the error on a half domain.

Let M_∞ be the Mach number of the flow at infinity, the potential flow is naturally expressed in the previous polar coordinates as:

$$\boldsymbol{v_0} := M_\infty \left[\left(1 - \frac{R_C^2}{r^2}\right) \cos\theta \boldsymbol{e}_r - \left(1 + \frac{R_C^2}{r^2}\right) \sin\theta \boldsymbol{e}_\theta \right],$$

leading to the following expression in cartesian coordinates

$$\begin{aligned} \boldsymbol{v_0} = M_\infty \Bigg[& \left(\frac{x - x_C}{r} \left(1 - \frac{R_C^2}{r^2}\right) \cos\theta + \frac{y - y_C}{r} \left(1 + \frac{R_C^2}{r^2}\right) \sin\theta \right) \boldsymbol{e}_x \\ & + \left(\frac{y - y_C}{r} \left(1 - \frac{R_C^2}{r^2}\right) \cos\theta - \frac{x - x_C}{r} \left(1 + \frac{R_C^2}{r^2}\right) \sin\theta \right) \boldsymbol{e}_y \Bigg]. \end{aligned}$$

The configuration for this case is depicted in FIGURE 11.

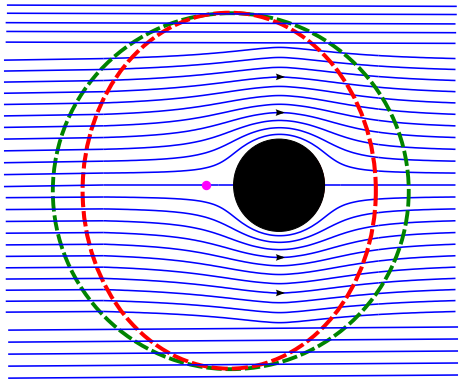

Figure 11: Sketch of the settings: in blue: streamlines of $\boldsymbol{v_0}$, in red: artificial boundary Σ, in green: artificial boundary in PGL coordinates, in magenta: point-source, in black: obstacle

In FIGURE 12, we plot p_h obtained with the following parameters

$$\boldsymbol{x}_C = (\pm 1, 0), \quad R_C = 0.5, \quad M_\infty = 0.4, \quad \omega = 6\pi.$$

It seems there is no reflection at the artificial boundary Σ and the expected physical phenomena are visible. We can clearly see a change in apparent frequency due to the Doppler effect, phase-shifts due to a refraction-like effect and an interference pattern due to the reflection of the wave on the obstacle. For the upstream example, we can also see a silent zone behind the obstacle as expected. For the downstream case, creeping waves can be seen around the obstacle, and a constructive interference pattern is visible behind the obstacle.

Similar cases to the upstream one have been studied in [BCD+14], the differences between the results obtained by the authors and our results may be explained by a different kind of source term and differences between 2D and 3D simulations. In particular, the pressure inside the silent cone is lower in our results.

Similar cases to the downstream one have been considered in [LMG+20]. The results obtained by the authors are very similar to the ones of this paper, therefore validating the new ABCs that we have constructed.

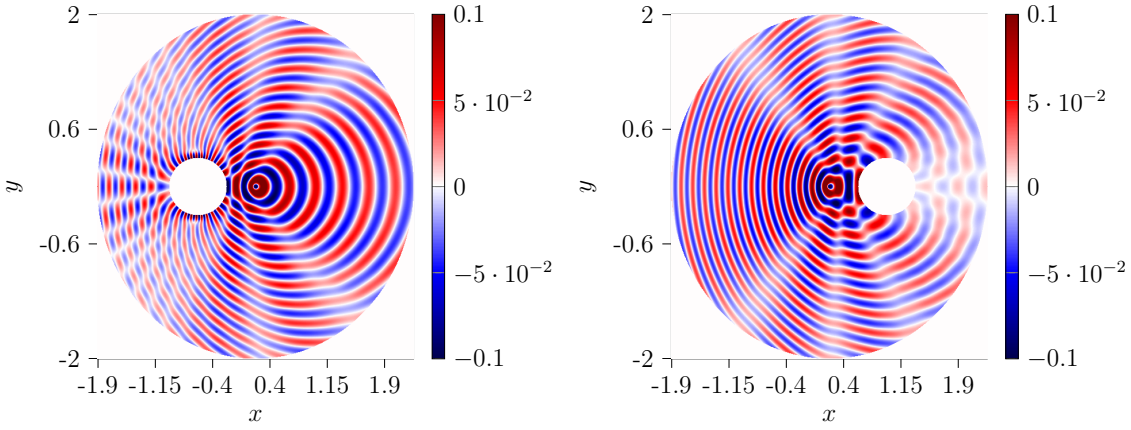

(a) Downstream obstacle

(b) Upstream obstacle

Figure 12: Point-source in a potential flow around a circular obstacle for $M_\infty = 0.4$

Conclusion

In this paper, we have seen that the use of the *Prandtl-Glauert-Lorentz transformation* to construct ABCs for the convected Helmholtz equation leads to very good results for low and intermediate Mach numbers. For higher Mach numbers, a very large domain seems to be required and the ABCs constructed in this paper should be used carefully. Due to the presence of convection, the usual idea of selecting waves that are locally orthogonal to the boundary leads to bad results, and the PGL-based ABCs should be preferred. Among those ABCs, the use of (ABC1) instead of (ABC0) gives better results for no additional cost. Finally we would like to point out that the ABCs constructed in this paper are really easy to implement in an existing finite-element solver for the convected Helmholtz equation as the PGL transformation is only required to compute the coefficient $\mathcal{Z}$.

When compared to other domain-truncation methods available in the literature, the PGL-based ABCs introduced in this paper have better performances than other low-order ABCs introduced *eg.* in [Gab03, Bér08]. As it can be expected, more advanced techniques such as the infinite elements [AH01], stabilized PMLs [MBAG21] or high-order ABCs [HHT03] can lead to better numerical results. In particular, those methods could be efficient to deal with high Mach numbers. But the integration of more sophisticated truncation methods in HDG formulations turns out to be a challenging work that is beyond the scope of this paper. By showing that HDG formulations can be coupled with ABCs for the convected Helmholtz equation, we have achieved an important start in the construction of advanced numerical methods for solving convected time harmonic wave equations posed in large domains.

Perspectives. The extension of this work to 3D is straightforward as the result of Theorem 4 relating $\mathcal{Z}$ to $\widetilde{\mathcal{Z}}$ holds for any dimension.

Extension of this work to higher order boundary conditions should be possible, we have already provided the expression of a second-order ABC. This is really an interesting purpose, as it was shown in [HHT03]. High-order ABCs seem to efficiently deal with problems involving large Mach numbers. But implementation of high order ABCs in HDG formulations is a non-trivial process, therefore rendering low-order ABCs attractive.

Extension to more realistic aeroacoustic models seem also possible. The most straightforward model to consider for this extension is Goldstein's equation [MMMP17] which consists in a coupling between a convected Helmholtz equation and a vectorial transport equation. The ABCs of this paper could be used for the convected Helmholtz equation and it is possible to obtain an exact outgoing condition for the transport equation. The extension to the Linearized Euler's Equations (LEE) [BBJ02] or Galbrun's equation [BMM+12] should also be feasible. Indeed, for a uniform flow those equations are equivalent to the convected Helmholtz equation, and it is therefore possible to construct ABCs for LEE from ABCs for the convected Helmholtz equation. A similar process was already carried out in [BT82] to compute steady-state solutions of the Euler's equations.

Acknowledgement

The authors would like to thank Florian Faucher for his help with the numerical implementation of HDG formulations with ABCs in `hawen`. The authors are also very thankful to the anonymous reviewers whose comments helped improve and clarify this manuscript.

Experiments presented in this paper were carried out using the PlaFRIM experimental testbed, supported by Inria, CNRS (LABRI and IMB), Université de Bordeaux, Bordeaux INP and Conseil Régional d'Aquitaine (see https://www.plafrim.fr).

Funding

Nathan Rouxelin was supported by a grant from e2s-UPPA (see https://e2s-uppa.eu).

Appendix A. Proof of Lemma 2

In this appendix, we prove the result of Lemma 2. As the numerical examples of this paper are in 2D, we have chosen to prove the result in the same dimension. Extension to 3D is straightforward and would involve the standard 3D Green functions instead of the Hankel functions.

We apply the *limiting amplitude principle* which consists in studying the long-term behaviour of the time-domain solution with the following source term

$$g(\boldsymbol{x}, t) = \begin{cases} s(\boldsymbol{x}) e^{-i\omega t}, & \text{if } t > 0 \\ 0, & \text{if } t \leqslant 0 \end{cases},$$

where s is a function in $L^2(\mathcal{O})$ with compact support.

As we are now working in time-domain, we recall that the space-time *Prandtl-Glauert-Lorentz transformation* reads

$$\widetilde{t} = \alpha t + \frac{\boldsymbol{M_0}\cdot\boldsymbol{x}}{\alpha c_0} \quad ; \quad \widetilde{\boldsymbol{x}} = \boldsymbol{A}\boldsymbol{x} := \left(\mathbf{Id} + \frac{1}{\alpha(1+\alpha)}\boldsymbol{M_0}\boldsymbol{M_0}^T\right)\boldsymbol{x},$$

see [HPN19]. The solutions to the convected wave equation and to the standard wave equations are linked by the following lemma.

Lemma 5. *If c_0 and $\boldsymbol{v_0}$ are constant, the quantity*

$$\widetilde{\mathsf{p}}(\widetilde{\boldsymbol{x}},\widetilde{t}) := \mathsf{p}(\boldsymbol{x},t),$$

satisfies the following wave equation

$$\partial^2_{\widetilde{t}\widetilde{t}}\widetilde{\mathsf{p}} - c_0^2\widetilde{\Delta}\widetilde{\mathsf{p}} = \widetilde{s},$$

where $\widetilde{\Delta}$ is the Laplace operator with respect to $\widetilde{\boldsymbol{x}}$ and $(\widetilde{\boldsymbol{x}},\widetilde{t})$ is defined by (6).

Step 1: Green functions in time-domain.
The Green function for the two-dimensional acoustic wave-equation in time-domain reads

$$G_{\text{std}}(\boldsymbol{x},t) = \frac{H\left(t-\frac{r}{c_0}\right)}{2\pi\sqrt{t^2-\frac{r^2}{c_0^2}}},$$

where H is the Heaviside function and $r = |\boldsymbol{x}|$. For the proof, we refer to [DJ06, Th. 1] or [Ver10, Sec. A.4.2].

The Green function for the convected wave equation in time-domain has been computed in the case $\boldsymbol{M_0} = M\boldsymbol{e}_x$ using the *Cagniard-de Hoop method* in [DJ06, Th. 6]. The case of a generic $\boldsymbol{M_0}$ reduces to this one by rotation. In this paper, the parameter σ denotes the absorption parameter used in PMLs, so we take $\sigma = 0$ leading to $A = B = 0$.

With the assumption that $\boldsymbol{M_0} = M\boldsymbol{e}_x$, the *Prandtl-Glauert-Lorentz transformation* reads

$$\widetilde{t} = \alpha t + \frac{1}{\alpha c_0}Mx, \quad \widetilde{x} = \frac{x}{\alpha}, \quad \widetilde{y} = y, \quad \widetilde{r}^2 = \widetilde{x}^2 + \widetilde{y}^2, \quad \widetilde{\theta} = \arctan\frac{\widetilde{y}}{\widetilde{x}}. \tag{A.1}$$

We define the following change of variables in space

$$\hat{x} = \frac{\widetilde{x}}{\alpha}, \quad \text{and} \quad \hat{y} = \frac{\widetilde{y}}{\alpha}. \tag{A.2a}$$

In polar coordinates, we also define

$$\hat{r}^2 = \hat{x}^2 + \hat{y}^2, \quad \text{and} \quad \hat{\theta} = \arctan\frac{\hat{y}}{\hat{x}}. \tag{A.2b}$$

It is straightforward to check that

$$\hat{r} = \frac{\widetilde{r}}{\alpha}, \quad \text{and} \quad \hat{\theta} = \widetilde{\theta}.$$

The Green function corresponding to the convected acoustic wave equation reads

$$G_{\text{conv}}(\boldsymbol{x}, t) = \frac{H(t - \frac{\hat{r}}{c_0}(1 - M\cos\hat{\theta}))}{2\pi\sqrt{1-M^2}\sqrt{(t + \frac{M\hat{r}}{c_0}\cos\hat{\theta})^2 - \frac{\hat{r}^2}{c_0}}}.$$

Using the intermediate change of variables (A.2a)–(A.2b) and expressing in terms of the *Prandt-Glauert-Lorentz coordinates* (A.1), we have

$$G_{\text{conv}}(\boldsymbol{x}, t) = \frac{H\left(t + \frac{M}{c_0}\hat{x} - \frac{\hat{r}}{c_0}\right)}{2\pi\alpha\sqrt{(t + \frac{M}{c_0}\hat{x})^2 - \frac{\hat{r}^2}{c_0^2}}} = \frac{H\left(\widetilde{t} - \frac{\widetilde{r}}{c_0}\right)}{2\pi\sqrt{\widetilde{t}^2 - \frac{\widetilde{r}^2}{c_0^2}}} = G_{\text{std}}(\widetilde{\boldsymbol{x}}, \widetilde{t}).$$

As G_{conv} is mapped to G_{std} through the *Prandtl-Glauert-Lorentz transformation*, we can therefore prove that this transform also maps outgoing solutions to outgoing solutions by using standard arguments of the *limiting amplitude principle*.

Step 2: Limiting amplitude principle for the standard Helmholtz equation.

We recall that the following identities hold

$$\int_r^{+\infty} \frac{e^{i\omega t}}{2\pi\sqrt{t^2 - r^2}}\mathrm{d}t = \frac{1}{2\pi}\int_0^{+\infty} e^{i\omega r\cosh\theta}\mathrm{d}\theta = \frac{i}{4}H_0^{(1)}(\omega r), \tag{A.3}$$

where we have used the following change of variables $t = r\cosh\theta$ and the integral form of the Hankel function, see [OLBC10, Eq. 10.9.10].

Using the integral representation we have

$$p_{\text{std}}(\boldsymbol{x}, t) = \int_{\mathbb{R}^2}\int_{\mathbb{R}} G_{\text{std}}(\boldsymbol{x}_1, t_1)g(\boldsymbol{x} - \boldsymbol{x}_1, t - t_1)\mathrm{d}t_1\mathrm{d}\boldsymbol{x}_1,$$

using the integral identity (A.3) for the Hankel function, we get

$$= \int_{\mathbb{R}^2}\int_{\frac{|\boldsymbol{x}_1|}{c_0}}^{+\infty} \frac{g(\boldsymbol{x} - \boldsymbol{x}_1, t - t_1)}{2\pi\sqrt{t_1^2 - \frac{|\boldsymbol{x}_1|^2}{c_0^2}}}\mathrm{d}t_1\mathrm{d}\boldsymbol{x}_1$$

using that $g(\boldsymbol{x}, t) = s(\boldsymbol{x})e^{-i\omega t}H(t)$, where s is a L^2-function with compact support,

$$= \int_{\mathbb{R}^2} s(\boldsymbol{x} - \boldsymbol{x}_1)e^{-i\omega t}\int_{\frac{|\boldsymbol{x}_1|}{c_0}}^{t} \frac{e^{i\omega t_1}}{2\pi\sqrt{t_1^2 - \frac{|\boldsymbol{x}_1|^2}{c_0^2}}}\mathrm{d}t_1\mathrm{d}\boldsymbol{x}_1$$

$$= \int_{\mathbb{R}^2} s(\boldsymbol{x} - \boldsymbol{x}_1)e^{-i\omega t}\left[\frac{i}{4}H_0^{(1)}\left(\frac{\omega}{c_0}|\boldsymbol{x}_1|\right) + \mathfrak{r}_{\text{std}}\right]\mathrm{d}\boldsymbol{x}_1$$

where $\mathfrak{r}_{\rm std}(\boldsymbol{x}_1,t) = -\displaystyle\int_t^{+\infty} \frac{e^{i\omega t_1}}{2\pi\sqrt{t_1^2-\frac{|\boldsymbol{x}_1|^2}{c_0^2}}}\mathrm{d}t_1$ with $t > \frac{|\boldsymbol{x}_1|}{c_0}$,

$$= \int_{\mathbb{R}^2} s(\boldsymbol{x}-\boldsymbol{x}_1)e^{-i\omega t}\frac{i}{4}H_0^{(1)}\left(\frac{\omega}{c_0}|\boldsymbol{x}_1|\right)\mathrm{d}\boldsymbol{x}_1 + \mathfrak{R}_{\rm std},$$

and

$$\mathfrak{R}_{\rm std}(\boldsymbol{x},t) = e^{-i\omega t}\int_{\mathbb{R}^2} s(\boldsymbol{x}-\boldsymbol{x}_1)\mathfrak{r}_{\rm std}(\boldsymbol{x}_1,t)\mathrm{d}\boldsymbol{x}_1 = -e^{-i\omega t}\int_{\mathbb{R}^2} s(\boldsymbol{x}-\boldsymbol{x}_1)\int_t^{+\infty}\frac{e^{i\omega t_1}}{2\pi\sqrt{t_1^2-\frac{|\boldsymbol{x}_1|^2}{c_0^2}}}\mathrm{d}t_1\mathrm{d}\boldsymbol{x}_1.$$

We now prove that $\mathfrak{R}_{\rm std}(\boldsymbol{x},t) \xrightarrow[t\to+\infty]{} 0$. The first step is to show that the integral defining $\mathfrak{r}_{\rm std}$ is actually finite-valued. We have

$$\begin{aligned}
\mathfrak{r}_{\rm std}(\boldsymbol{x}_1,t) &:= -\int_t^{+\infty}\frac{e^{i\omega t_1}}{2\pi\sqrt{t_1^2-\frac{|\boldsymbol{x}_1|^2}{c_0^2}}}\mathrm{d}t_1 \\
&= -\lim_{A\to+\infty}\left(\left[\frac{e^{i\omega t_1}}{2i\pi\omega\sqrt{t_1^2-\frac{|\boldsymbol{x}_1|^2}{c_0^2}}}\right]_t^A + \int_t^A \frac{t_1 e^{i\omega t_1}}{2\pi\left(t_1^2-\frac{|\boldsymbol{x}_1|^2}{c_0^2}\right)^{\frac{3}{2}}}\mathrm{d}t_1\right) \\
&< +\infty,
\end{aligned}$$

as

$$\lim_{A\to+\infty}\frac{e^{i\omega A}}{2i\pi\omega\sqrt{A^2-\frac{|\boldsymbol{x}_1|^2}{c_0^2}}} = 0, \quad \text{and} \quad \left|\frac{t_1 e^{i\omega t_1}}{2\pi\left(t_1^2-\frac{|\boldsymbol{x}_1|^2}{c_0^2}\right)^{\frac{3}{2}}}\right| = \frac{t_1}{2\pi\left(t_1^2-\frac{|\boldsymbol{x}_1|^2}{c_0^2}\right)^{\frac{3}{2}}} \underset{t_1\to\infty}{\sim} \frac{1}{t_1^2}.$$

We can therefore express $\mathfrak{r}_{\rm std}$ as

$$\mathfrak{r}_{\rm std}(\boldsymbol{x}_1,t) = -\frac{e^{i\omega t}}{2i\pi\omega\sqrt{t^2-\frac{|\boldsymbol{x}_1|^2}{c_0^2}}} - \int_t^{+\infty}\frac{t_1 e^{i\omega t_1}}{2\pi\left(t_1^2-\frac{|\boldsymbol{x}_1|^2}{c_0^2}\right)^{\frac{3}{2}}}\mathrm{d}t_1$$

and $\mathfrak{R}_{\rm std}$ as

$$\mathfrak{R}_{\rm std}(\boldsymbol{x},t) = \int_{\mathbb{R}^2}\frac{s(\boldsymbol{x}-\boldsymbol{x}_1)}{2\pi\sqrt{t^2-\frac{|\boldsymbol{x}_1|^2}{c_0^2}}}\mathrm{d}\boldsymbol{x}_1 + e^{-i\omega t}\int_{\mathbb{R}^2} s(\boldsymbol{x}-\boldsymbol{x}_1)\int_t^{+\infty}\frac{t_1 e^{i\omega t_1}}{2\pi\left(t_1^2-\frac{|\boldsymbol{x}_1|^2}{c_0^2}\right)^{\frac{3}{2}}}\mathrm{d}t_1\mathrm{d}\boldsymbol{x}_1.$$

We can now show that both of these quantities vanish at infinity. Let us first focus on the first term in $\mathfrak{R}_{\rm std}$

$$\int_{\mathbb{R}^2}\frac{s(\boldsymbol{x}-\boldsymbol{x}_1)}{2\pi\sqrt{t^2-\frac{|\boldsymbol{x}_1|^2}{c_0^2}}}\mathrm{d}\boldsymbol{x}_1.$$

As we are interested in the limit as $t \to +\infty$ and as the space integral is over a compact domain, we can assume that

$$\frac{3t^2}{4} > \frac{|\boldsymbol{x}_1|^2}{c_0^2},$$

which leads to

$$\frac{|s(\boldsymbol{x}-\boldsymbol{x}_1)|}{2\pi\sqrt{t^2-\frac{|\boldsymbol{x}_1|^2}{c_0^2}}} < \frac{|s(\boldsymbol{x}-\boldsymbol{x}_1)|}{\pi|t|},$$

and we have

$$\int_{\mathbb{R}^2}\left|\frac{s(\boldsymbol{x}-\boldsymbol{x}_1)}{2\pi\sqrt{t^2-\frac{|\boldsymbol{x}_1|^2}{c_0^2}}}\right|\mathrm{d}\boldsymbol{x}_1 \leqslant \frac{1}{\pi|t|}\int_{\mathbb{R}^2}|s(\boldsymbol{x}-\boldsymbol{x}_1)|\mathrm{d}\boldsymbol{x}_1 \xrightarrow[t\to+\infty]{} 0,$$

as the last integral is over a compact domain. By taking the limit in the previous inequality, we have

$$\lim_{t\to+\infty}\int_{\mathbb{R}^2}\left|\frac{s(\boldsymbol{x}-\boldsymbol{x}_1)}{2\pi\sqrt{t^2-\frac{|\boldsymbol{x}_1|^2}{c_0^2}}}\right|\mathrm{d}\boldsymbol{x}_1 = 0.$$

We can now work on the second term.

As we are interested in the limit as $t \to +\infty$ and as the space integral is over a compact domain, we can assume once again that

$$\frac{3t_1^2}{4} > \frac{3t^2}{4} > \frac{|\boldsymbol{x}_1|^2}{c_0^2},$$

which leads to

$$\frac{t_1}{2\pi\left(t_1^2-\frac{|\boldsymbol{x}_1|^2}{c_0^2}\right)^{\frac{3}{2}}} < \frac{t_1}{\frac{\pi}{4}t_1^3} = \frac{4}{\pi t_1^2}.$$

We therefore have

$$\int_t^{+\infty}\left|\frac{t_1 e^{i\omega t_1}}{2\pi\left(t_1^2-\frac{|\boldsymbol{x}_1|^2}{c_0^2}\right)^{\frac{3}{2}}}\right|\mathrm{d}t_1 < \frac{4}{\pi}\int_t^{+\infty}\frac{1}{t_1^2}\mathrm{d}t_1 = \frac{4}{\pi t} \xrightarrow[t\to+\infty]{} 0.$$

Finally we have

$$\begin{aligned}\int_{\mathbb{R}^2}|s(\boldsymbol{x}-\boldsymbol{x}_1)|\int_t^{+\infty}\left|\frac{t_1 e^{i\omega t_1}}{2\pi\left(t_1^2-\frac{|\boldsymbol{x}_1|^2}{c_0^2}\right)^{\frac{3}{2}}}\right|\mathrm{d}t_1\mathrm{d}\boldsymbol{x}_1 &\leqslant \int_{\mathbb{R}^2}|s(\boldsymbol{x}-\boldsymbol{x}_1)|\frac{4}{\pi t}\mathrm{d}\boldsymbol{x}_1 \\ &\leqslant \frac{4}{\pi t}\int_{\mathbb{R}^2}|s(\boldsymbol{x}-\boldsymbol{x}_1)|\mathrm{d}\boldsymbol{x}_1 \xrightarrow[t\to+\infty]{} 0.\end{aligned}$$

Notice that the last integral is finite as the support of s is compact. By taking the limit in the previous inequalities, we have

$$\lim_{t\to+\infty}\int_{\mathbb{R}^2}|s(\boldsymbol{x}-\boldsymbol{x}_1)|\int_t^{+\infty}\left|\frac{t_1 e^{i\omega t_1}}{2\pi\left(t_1^2-\frac{|\boldsymbol{x}_1|^2}{c_0^2}\right)^{\frac{3}{2}}}\right|\mathrm{d}t_1\mathrm{d}\boldsymbol{x}_1=0.$$

We therefore have

$$\lim_{t\to+\infty}|\mathfrak{R}_{\mathrm{std}}(\boldsymbol{x},t)|=0,\quad\forall\boldsymbol{x}\in\mathbb{R}^2.$$

Now, we define the time-harmonic Green function by

$$W_{\mathrm{std}}(\boldsymbol{x},\omega)=\frac{i}{4}H_0^{(1)}\left(\frac{\omega}{c_0}|\boldsymbol{x}|\right).$$

We end up with the *limiting amplitude principle*

$$\lim_{t\to\infty}\left\|p_{\mathrm{std}}(\boldsymbol{x},t)-p_{\mathrm{std},\omega}(\boldsymbol{x})e^{-i\omega t}\right\|_{L^2(\mathbb{R}^2)}=0,$$

where $p_{\mathrm{std},\omega}:=W_{\mathrm{std}}(\cdot,\omega)*s$ is the outgoing solution of the standard Helmholtz equation.

Step 3: Limiting amplitude principle for the convected Helmholtz equation. We have

$$\begin{aligned}
p(\boldsymbol{x},t)&=\int_{\mathbb{R}^2}\int_{\mathbb{R}}G_{\mathrm{conv}}(\boldsymbol{x}_1,t_1)g(\boldsymbol{x}-\boldsymbol{x}_1,t-t_1)\mathrm{d}t_1\mathrm{d}\boldsymbol{x}_1\\
&=\int_{\mathbb{R}^2}\int_{\mathbb{R}}G_{\mathrm{std}}(\widetilde{\boldsymbol{x}}_1,\widetilde{t}_1)g\left(\boldsymbol{A}^{-1}(\widetilde{\boldsymbol{x}}-\widetilde{\boldsymbol{x}}_1),\frac{1}{\alpha}(\widetilde{t}-\widetilde{t}_1)+\frac{1}{\alpha c_0}\boldsymbol{M_0}\cdot(\widetilde{\boldsymbol{x}}-\widetilde{\boldsymbol{x}}_1)\right)\mathrm{d}\widetilde{t}_1\mathrm{d}\widetilde{\boldsymbol{x}}_1\\
&=\int_{\mathbb{R}^2}\int_{\frac{|\widetilde{\boldsymbol{x}}_1|}{c_0}}^{+\infty}\frac{g\left(\boldsymbol{A}^{-1}(\widetilde{\boldsymbol{x}}-\widetilde{\boldsymbol{x}}_1),\frac{1}{\alpha}(\widetilde{t}-\widetilde{t}_1)-\frac{1}{\alpha c_0}\boldsymbol{M_0}\cdot(\widetilde{\boldsymbol{x}}-\widetilde{\boldsymbol{x}}_1)\right)}{2\pi\sqrt{\widetilde{t}_1^2-\frac{|\widetilde{\boldsymbol{x}}_1|^2}{c_0^2}}}\mathrm{d}\widetilde{t}_1\mathrm{d}\widetilde{\boldsymbol{x}}_1
\end{aligned}$$

using that $g(\boldsymbol{x},t)=s(\boldsymbol{x})e^{-i\omega t}H(t)$, where s is a function with compact support,

$$=\int_{\mathbb{R}^2}s(\boldsymbol{A}^{-1}(\widetilde{\boldsymbol{x}}-\widetilde{\boldsymbol{x}}_1))e^{-i\omega(\frac{1}{\alpha}\widetilde{t}-\frac{1}{\alpha c_0}\boldsymbol{M_0}\cdot\widetilde{\boldsymbol{x}})}e^{-i\frac{\omega}{\alpha c_0}\boldsymbol{M_0}\cdot\widetilde{\boldsymbol{x}}_1}\int_{\frac{|\widetilde{\boldsymbol{x}}_1|}{c_0}}^{\widetilde{t}-\frac{\boldsymbol{M_0}}{c_0}\cdot(\widetilde{\boldsymbol{x}}-\widetilde{\boldsymbol{x}}_1)}\frac{e^{i\frac{\omega}{\alpha}\widetilde{t}}}{2\pi\sqrt{\widetilde{t}_1^2-\frac{|\widetilde{\boldsymbol{x}}_1|^2}{c_0^2}}}\mathrm{d}\widetilde{t}_1\mathrm{d}\widetilde{\boldsymbol{x}}_1$$

$$\begin{aligned}
&=\int_{\mathbb{R}^2}s(\boldsymbol{A}^{-1}(\widetilde{\boldsymbol{x}}-\widetilde{\boldsymbol{x}}_1))e^{-i\omega(\frac{1}{\alpha}\widetilde{t}-\frac{1}{\alpha c_0}\boldsymbol{M_0}\cdot\widetilde{\boldsymbol{x}})}e^{-i\frac{\omega}{\alpha c_0}\boldsymbol{M_0}\cdot\widetilde{\boldsymbol{x}}_1}\left[\frac{i}{4}H_0^{(1)}\left(\frac{\omega}{\alpha c_0}|\widetilde{\boldsymbol{x}}_1|\right)+\mathfrak{r}_{\mathrm{conv}}\right]\mathrm{d}\widetilde{\boldsymbol{x}}_1\\
&=\int_{\mathbb{R}^2}\frac{1}{\alpha}s(\boldsymbol{x}-\boldsymbol{x}_1)e^{-i\omega t}e^{-i\frac{\omega}{\alpha^2 c_0}\boldsymbol{M_0}\cdot\boldsymbol{x}_1}\frac{i}{4}H_0^{(1)}\left(\frac{\omega}{\alpha c_0}|\boldsymbol{A}\boldsymbol{x}_1|\right)\mathrm{d}\boldsymbol{x}_1+\mathfrak{R}_{\mathrm{conv}},
\end{aligned}$$

where $\mathfrak{r}_{\mathrm{conv}}$ and $\mathfrak{R}_{\mathrm{conv}}$ are defined as $\mathfrak{r}_{\mathrm{std}}$ and $\mathfrak{R}_{\mathrm{std}}$ in the previous step. By using similar arguments to the ones in the previous step, we can show that

$$\lim_{t\to+\infty}\|\mathfrak{R}_{\mathrm{conv}}(\cdot,t)\|=0.$$

We now define the time-harmonic Green function by

$$W_{\text{conv}}(\boldsymbol{x},\omega) = \frac{1}{\alpha}\exp\left[-\frac{i\omega}{\alpha^2 c_0}\boldsymbol{M_0}\cdot\boldsymbol{x}\right]\frac{i}{4}H_0^{(1)}\left(\frac{\omega}{\alpha c_0}|\boldsymbol{A}\boldsymbol{x}|\right),$$

and we can also obtain the limiting amplitude principle for the convected Helmholtz equation

$$\lim_{t\to\infty}\left\|p(\boldsymbol{x},t) - p_{\text{conv},\omega}(\boldsymbol{x})e^{-i\omega t}\right\|_{L^2(\mathbb{R}^2)} = 0,$$

where $p_{\text{conv},\omega} = W_{\text{conv}}(\cdot,\omega) * s$ is the outgoing solution of the convected Helmholtz equation.

Step 4: Equivalence under *Prandtl-Glauert-Lorentz transformation.*

We notice that

$$W_{\text{conv}}(\boldsymbol{x},\omega) = \frac{1}{\alpha}\exp\left[-\frac{i\omega}{\alpha^2 c_0}\boldsymbol{M_0}\cdot\boldsymbol{x}\right]\frac{i}{4}H_0^{(1)}\left(\frac{\omega}{\alpha c_0}|\boldsymbol{A}\boldsymbol{x}|\right) = \frac{1}{\alpha}\exp\left[-\frac{i\omega}{\alpha^2 c_0}\boldsymbol{M_0}\cdot\boldsymbol{x}\right]W_{\text{std}}\left(\widetilde{\boldsymbol{x}},\frac{\omega}{\alpha}\right),$$

We recall that $\widetilde{s}$ is defined by

$$\widetilde{s}(\widetilde{\boldsymbol{x}},\widetilde{\omega}) := \alpha\exp\left[i\omega\frac{\boldsymbol{M_0}\cdot\boldsymbol{x}}{\alpha^2 c_0}\right]s(\boldsymbol{x},\omega),$$

and we define

$$\widetilde{p}_{\text{std},\widetilde{\omega}} := W_{\text{std}}(\cdot,\widetilde{\omega}) * \widetilde{s} = \int_{\mathbb{R}^2}\widetilde{s}(\cdot-\widetilde{\boldsymbol{x}}_1)W_{\text{std}}(\widetilde{\boldsymbol{x}}_1,\widetilde{\omega})\mathrm{d}\widetilde{\boldsymbol{x}}_1.$$

We have

$$\widetilde{p}_{\text{std},\widetilde{\omega}}(\widetilde{\boldsymbol{x}}) = \alpha\exp\left[i\omega\frac{\boldsymbol{M_0}\cdot\boldsymbol{x}}{\alpha^2 c_0}\right]p_{\text{conv},\omega}(\boldsymbol{x}),$$

indeed

$$\begin{aligned}
\widetilde{p}_{\text{std},\widetilde{\omega}}(\widetilde{\boldsymbol{x}}) &= \int_{\mathbb{R}^2}\widetilde{s}(\widetilde{\boldsymbol{x}}-\widetilde{\boldsymbol{x}}_1)W_{\text{std}}(\widetilde{\boldsymbol{x}}_1,\widetilde{\omega})\mathrm{d}\widetilde{\boldsymbol{x}}_1,\\
&= \int_{\mathbb{R}^2}\alpha\exp\left[i\omega\frac{\boldsymbol{M_0}\cdot(\boldsymbol{x}-\boldsymbol{x}_1)}{\alpha^2 c_0}\right]s(\boldsymbol{x}-\boldsymbol{x}_1)\alpha\exp\left[i\omega\frac{\boldsymbol{M_0}\cdot\boldsymbol{x}_1}{\alpha^2 c_0}\right]W_{\text{conv}}(\boldsymbol{x}_1,\omega)\frac{\mathrm{d}\boldsymbol{x}_1}{\alpha},\\
&= \alpha\exp\left[i\omega\frac{\boldsymbol{M_0}\cdot\boldsymbol{x}}{\alpha^2 c_0}\right]\int_{\mathbb{R}^2}s(\boldsymbol{x}-\boldsymbol{x}_1)W_{\text{conv}}(\boldsymbol{x}_1,\omega)\mathrm{d}\boldsymbol{x}_1.
\end{aligned}$$

So the outgoing solutions are mapped to one another through the *Prandtl-Glauert-Lorentz transformation.*

[ABB99] Xavier Antoine, Helene Barucq, and Abderrahmane Bendali. Bayliss-Turkel-like Radiation Condition on Surfaces of Arbitrary Shape. *Journal of Mathematical Analysis and Applications*, 229(1):184–211, 1999. Cited on pages 8 and 15.

[AH01] R. Jeremy Astley and James A. Hamilton. Infinite elements for transient flow acoustics | 7th AIAA/CEAS Aeroacoustics Conference and Exhibit. https://arc.aiaa.org/doi/abs/10.2514/6.2001-2273, 2001. Cited on pages 3, 24, and 26.

[BBJ02] Christophe Bogey, Christophe Bailly, and Daniel Juvé. Computation of Flow Noise Using Source Terms in Linearized Euler's Equations. *Aiaa Journal - AIAA J*, 40:235–243, February 2002. Cited on page 27.

[BCD+14] Nolwenn Balin, Fabien Casenave, Francois Dubois, Eric Duceau, Stefan Duprey, and Isabelle Terrasse. Boundary Element and Finite Element Coupling for Aeroacoustics Simulations. Technical report, February 2014. Cited on pages 3 and 25.

[BDL04] Eliane Bécache, AS Bonnet-Ben Dhia, and Guillaume Legendre. Perfectly matched layers for the convected helmholtz equation. *SIAM Journal on Numerical Analysis*, 42(1):409–433, 2004. Cited on pages 2 and 21.

[Ber94] Jean-Pierre Berenger. A perfectly matched layer for the absorption of electromagnetic waves. *Journal of Computational Physics*, 114(2):185–200, October 1994. Cited on page 2.

[Bér08] Hadrien Bériot. *Eléments Finis d'ordre Élévé Pour l'opérateur de Galbrun En Régime Harmonique*. Thesis, Compiègne, January 2008. Cited on pages 22 and 26.

[BGH10] Eliane Bécache, Dan Givoli, and Thomas Hagstrom. High-order Absorbing Boundary Conditions for anisotropic and convective wave equations. *Journal of Computational Physics*, 229(4):1099–1129, 2010. Cited on pages 2, 3, and 15.

[BGT82] Alvin Bayliss, Max Gunzburger, and Eli Turkel. Boundary conditions for the numerical solution of elliptic equations in exterior regions. *SIAM Journal on Applied Mathematics*, 42:430–451, 1982. Cited on pages 3, 8, 11, and 12.

[BMM+12] Anne-Sophie Bonnet-Ben Dhia, Jean-François Mercier, Florence Millot, Sebastien Pernet, and Emilie Peynaud. Time-Harmonic Acoustic Scattering in a Complex Flow: A Full Coupling Between Acoustics and Hydrodynamics. *Communications in Computational Physics*, 11(2):555–572, February 2012. Cited on page 27.

[BRT21] Helene Barucq, Nathan Rouxelin, and Sebastien Tordeux. HDG and HDG+ methods for harmonic wave problems with convection. 2021. Cited on pages 2, 3, 5, 8, 9, and 16.

[BST12] Helene Barucq, Anne-Gaelle St-Guirons, and Sebastien Tordeux. Non-reflecting boundary condition on ellipsoidal boundary. *Numerical Analysis and Applications*, 5(2):109–115, April 2012. Cited on page 8.

[BT82] Alvin Bayliss and Eli Turkel. Far field boundary conditions for compressible flows. *Journal of Computational Physics*, 48(2):182–199, November 1982. Cited on pages 3, 12, and 27.

[CES14] Fabien Casenave, Alexandre Ern, and Guillaume Sylvand. Coupled BEM–FEM for the convected Helmholtz equation with non-uniform flow in a bounded domain. *Journal of Computational Physics*, 257:627–644, January 2014. Cited on page 3.

[Cha00] C. John Chapman. Similarity variables for sound radiation in a uniform flow. *Journal of Sound and Vibration*, 233(1):157–164, 2000. Cited on page 6.

[DDMT11] François Dubois, Eric Duceau, Frédéric Marechal, and Isabelle Terrasse. Lorentz transform and staggered finite differences for advective acoustics. *arXiv preprint arXiv:1105.1458*, 2011. Cited on page 2.

[DJ06] Julien Diaz and Patrick Joly. A time domain analysis of PML models in acoustics. *Computer Methods in Applied Mechanics and Engineering*, 195(29-32):3820–3853, June 2006. Cited on page 28.

[Dup11] Véronique Duprat. *Conditions Aux Limites Absorbantes Enrichies Pour l'équation Des Ondes Acoustiques et l'équation d'Helmholtz*. These de doctorat, Pau, December 2011. Cited on page 10.

[EM77] Bjorn Engquist and Andrew Majda. Absorbing Boundary Conditions for the Numerical Simulation of Waves. *Mathematics of Computation*, page 23, 1977. Cited on page 2.

[Fau21] Florian Faucher. 'hawen': Time-harmonic wave modeling and inversion using hybridizable discontinuous Galerkin discretization. *Journal of Open Source Software*, 6(57):2699, January 2021. Cited on page 16.

[Gab03] Gwenael Gabard. *Méthodes Numériques et Modèles de Sources Aéroacoustiques Fondées Sur l'équation de Galbrun*. PhD thesis, 2003. Cited on pages 22 and 26.

[HHT03] Thomas Hagstrom, S. I. Hariharan, and David Thompson. High-Order Radiation Boundary Conditions for the Convective Wave Equation in Exterior Domains. *Siam Journal on Scientific Computing*, 25, November 2003. Cited on pages 2, 3, 15, 20, 22, 26, and 27.

[HN02] Thomas Hagstrom and Igor Nazarov. Absorbing layers and radiation boundary conditions for jet flow simulations. In *8th AIAA/CEAS Aeroacoustics Conference & Exhibit*, page 2606, 2002. Cited on page 2.

[HPN17] Fang Q. Hu, Michelle E. Pizzo, and Douglas M. Nark. On a time domain boundary integral equation formulation for acoustic scattering by rigid bodies in uniform mean flow. *The Journal of the Acoustical Society of America*, 142(6):3624, December 2017. Cited on page 10.

[HPN19] Fang Q. Hu, Michelle E. Pizzo, and Douglas M. Nark. On the use of a Prandtl-Glauert-Lorentz transformation for acoustic scattering by rigid bodies with a uniform flow. *Journal of Sound and Vibration*, 443:198–211, March 2019. Cited on pages 6, 9, 10, and 28.

[Hu01] Fang Q Hu. A stable, perfectly matched layer for linearized euler equations in unsplit physical variables. *Journal of Computational Physics*, 173(2):455–480, 2001. Cited on page 2.

[Kim14] Seungil Kim. Analysis of the convected Helmholtz equation with a uniform mean flow in a waveguide with complete radiation boundary conditions. *Journal of Mathematical Analysis and Applications*, 410(1):275–291, February 2014. Cited on page 3.

[KSC12] Robert J. Kirby, Spencer J. Sherwin, and Bernardo Cockburn. To CG or to HDG: A Comparative Study. *Journal of Scientific Computing*, 51(1):183–212, April 2012. Cited on page 2.

[LMG+20] Alice Lieu, Philippe Marchner, Gwenael Gabard, Hadrien Beriot, Xavier Antoine, and Christophe Geuzaine. A Non-Overlapping Schwarz Domain Decomposition Method with High-Order Finite Elements for Flow Acoustics. *Computer Methods in Applied Mechanics and Engineering*, 2020. Cited on pages 10 and 25.

[MAGB21] Philippe Marchner, Xavier Antoine, Christophe Geuzaine, and Hadrien Bériot. Construction and Numerical Assessment of Local Absorbing Boundary Conditions for Heterogeneous Time-Harmonic Acoustic Problems. April 2021. Cited on page 3.

[MBAG21] Philippe Marchner, Hadrien Beriot, Xavier Antoine, and Christophe Geuzaine. Stable perfectly matched layers with lorentz transformation for the convected helmholtz equation. *Journal of Computational Physics*, 433:110180, 2021. Cited on pages 2, 6, 16, 21, and 26.

[MMMP17] Jean-François Mercier, Colin Mietka, Florence Millot, and Vincent Pagneux. Acoustic propagation in a vortical homentropic flow. page 19, 2017. Cited on page 27.

[OLBC10] Frank Olver, Daniel W. Lozier, Ronald F. Boisvert, and Charles W. Clark. NIST Handbook of Mathematical Functions. January 2010. Cited on page 29.

[Pie90] Allan Pierce. Wave equation for sound in fluids with unsteady inhomogeneous flow. *The Journal of the Acoustical Society of America*, 87(6):2292–2299, June 1990. Cited on page 4.

[Rou21] Nathan Rouxelin. *Mixed condensed numerical methods for convected wave propagation. Applications in helioseismology.* Thesis, 2021. Cited on pages 1 and 6.

[Sai08] Anne-Gaelle Saint-Guirons. *Construction et Analyse de Conditions Absorbantes de Type Diritchlet-to-Neumann Pour Des Frontières Ellipsoïdales.* PhD thesis, Pau, January 2008. Cited on page 8.

[SM50] Jack Sherman and Winifried Morrison. Adjustment of an Inverse Matrix Corresponding to a Change in One Element of a Given Matrix. *Annals of Mathematical Statistics*, 21(1):124–127, March 1950. Cited on page 6.

[Ver10] Arnold Verruijt. *An Introduction to Soil Dynamics.* Theory and Applications of Transport in Porous Media. Springer Netherlands, 2010. Cited on page 28.